Journal of Materials Chemistry C

ROYAL SOCIETY OF CHEMISTRY

PAPER

View Article Online
View Journal | View Issue

Cite this: J. Mater. Chem. C, 2025, 13, 13691

Received 4th April 2025,
Accepted 22nd May 2025

DOI: 10.1039/d5tc01411e

rsc.li/materials-c

Shaping scintillation and UV-VIS-NIR luminescence properties through synergistic lattice disordered engineering and exciton-mediated energy transfer in Pr^{3+}-doped $Lu_{1.5}Y_{1.5}Al_{5-x}Sc_xO_{12}$ (x = 0.0–2.0) garnets†

Karol Bartosiewicz,*[a] Yevheniia Smortsova,[b] Piotr Radmoski,[c] Marcin E. Witkowski,[d] Konrad J. Drozdowski,[d] Masao Yoshino,[ef] Takahiko Horiai,[ef] Damian Szymański,[g] Wioletta Dewo,[c] Justyna Zeler,[h] Paweł Socha,[i] Maksym Buryi,[j] Andrey Prokhorov,[aj] David John,[akl] Jakub Volf,[am] Tomasz Runka,[c] Tomasz Pędziński,[n] Karol Hauza,[n] Vítězslav Jarý,[a] Yasuhiro Shoji,[ef] Kei Kamada,[ef] Eugeniusz Zych,[h] Winicjusz Drozdowski[d] and Akira Yoshikawa[ef]

This study investigated the crystallization behavior, luminescence and scintillation properties of Pr^{3+}-doped $Lu_{1.5}Y_{1.5}Al_{5-x}Sc_xO_{12}$ (0.0, 0.5, 1.0, 1.5, 2.0) garnets, grown using the micro-pulling-down method, to address challenges associated with the substitution of Sc^{3+} for Al^{3+} ions due to their mismatched ionic radii in the same octahedral crystallographic site. A specially engineered crucible with five independent crystallization capillaries was used, which revealed that Sc^{3+} substitution caused localized melt heterogeneity, resulting in non-uniform melt ejection during crystallization. The threshold of Sc^{3+} ions concentration (x = 1.5) was identified, beyond which further substitution led to the formation of a

[a] Institute of Physics, Academy of Sciences of the Czech Republic, Na Slovance 1999/2, 18200, Prague, Czech Republic. E-mail: bartosiewicz@fzu.cz
[b] Deutsches Elektronen-Synchrotron DESY, Notkestr. 85, Hamburg 22607, Germany
[c] Faculty of Materials Engineering and Technical Physics, Poznan University of Technology, Piotrowo 3, 60-965, Poznań, Poland
[d] Institute of Physics, Faculty of Physics, Astronomy and Informatics, Nicolaus Copernicus University in Toruń, ul. Grudziądzka 5, 87100, Toruń, Poland
[e] Institute for Materials Research, Tohoku University, 2-1-1 Katahira Aoba-ku, Sendai, Miyagi 9808577, Japan
[f] New Industry Creation Hatchery Center, Tohoku University, Sendai, Miyagi, Japan
[g] Institute of Low Temperature and Structure Research, Polish Academy of Sciences, Wrocław, Poland
[h] Faculty of Chemistry, University of Wrocław, Joliot-Curie Street 14 F, 50383, Wrocław, Poland
[i] Łukasiewicz Research Network – Institute of Microelectronics and Photonics, Aleja Lotników 32/46, 02-668, Warsaw, Poland
[j] Institute of Plasma Physics of the Czech Academy of Sciences, U Slovanky, 2525/1a, Prague, 182 00, Czech Republic
[k] Faculty of Nuclear Sciences and Physical Engineering, Czech Technical University, Břehová 7, 115019, Prague, Czech Republic
[l] Nuclear Physics Institute of the Czech Academy of Sciences, Na Truhlářce 39/64, 18000, Prague, Czech Republic
[m] Department of Inorganic Chemistry, University of Chemistry and Technology, Technická 5, 166 28, Prague, Czech Republic
[n] Faculty of Chemistry, Adam Mickiewicz University in Poznań, Uniwersytetu Poznańskiego 8, 61-614 Poznan, Poland

† Electronic supplementary information (ESI) available: NIR-VIS-UV absorption spectra – Fig. S1 Room-temperature unpolarized optical absorption spectra of Pr^{3+}-doped $Lu_{1.5}Y_{1.5}Al_{5-x}Sc_xO_{12}$ (x = 0.0–2.0) in NIR, VIS, and UV regions. Raman spectroscopy characteristics – Table S1 Experimental Raman bands of Pr^{3+}-doped $Lu_{1.5}Y_{1.5}Al_{5-x}Sc_xO_{12}$ compared with $Y_3Al_5O_{12}$, including symmetry and vibrational modes. Thermal modification of photoluminescence characteristics – Fig. S2 2D temperature-dependent (10–350 K) emission and excitation maps for crystals with varying Sc concentrations. Fig. S3 Radial variation of PL intensity, emission line FWHM, and integrated spectral intensity as a function of Sc^{3+} content. Photoluminescence decay dynamics – Fig. S4 RT photoluminescence decay time curves and multi-exponential fitting analysis for Sc concentrations x = 0.5 and 1.5. Emission band characteristics – Table S2 Maximum band positions and FWHM of interconfigurational Pr^{3+} $4f^15d_1^1 \rightarrow 4f^2$ emission across various garnet matrices and Sc-admixed materials. Luminescence properties under synchrotron radiation – Fig. S5 2D excitation–emission maps at 8 K and 295 K for Sc concentrations of x = 0.5, 1.5, and 2.0, highlighting broadening and intensity trends in emission regions. Radioluminescence and scintillation properties – Fig. S6 Temperature-dependent (10–350 K) radioluminescence spectra for Pr^{3+}-doped $Lu_{1.5}Y_{1.5}Al_{5-x}Sc_xO_{12}$ with varying Sc concentrations. Fig. S7 (a) Scintillation light yield *vs.* Sc concentration and (b) decay kinetics under ^{137}Cs (662 keV) γ-ray excitation. Electron paramagnetic resonance (EPR) analysis – Fig. S8 (a) Charge trapping signals (S1–S5) as Sc concentration increases, (b) double integral intensities of signals, and (c) measured *vs.* calculated EPR spectra interpretation. Emission spectra under controlled excitation – Fig. S9 (a) Emission spectra for x = 0.0 and x = 2.0 at 8 K under 6.52 eV excitation, (b) Gaussian fits illustrating transitions, (c) dependence of fit intensities on Sc^{3+} ions concentration, (d) spectral evolution with increasing Sc^{3+} ions concentration. See DOI: https://doi.org/10.1039/d5tc01411e

garnet/bixbyite-like distorted perovskite hypoeutectic structure. This discovered a novel method for crystallization of hypoeutectic crystal growth by exploiting ionic radii mismatches. Vibrational spectroscopy confirmed that Sc^{3+} ions incorporation disrupted lattice symmetry, increasing structural disorder around Pr^{3+} ions. This structural modification significantly enhanced luminescence, particularly in the visible and near-infrared (NIR) ranges, achieving a sixteenfold increase in NIR luminescence intensity. Synchrotron radiation excitation spectra revealed that the band gap energy progressively decreased with increasing Sc^{3+} ions concentration. This finding provided crucial insights for designing materials based on band gap engineering strategies. A sixfold improvement in scintillation light yield, reaching 11 200 photons per MeV, was observed in the $Lu_{1.5}Y_{1.5}Al_{3.5}Sc_{1.5}O_{12}$ crystal (x = 1.5). The enhancement resulted from a Sc^{3+}-mediated energy transfer pathway $\left(Sc_{e^-\rightarrow h^+}{}^{3+} \rightarrow Pr^{3+}\right)$, which optimized charge carrier dynamics by reducing deep trapping center density by an order of magnitude while preserving shallow traps. The EPR spectroscopy showed that Sc^{3+} incorporation reduced concentration of trace impurities, enhancing scintillation light yield. It also confirmed that F^+–Pr^{3+} interactions intensified Pr^{3+} emission at 370 nm and identified the 410–420 nm band as originating from F^+–O^- defect pairs. These findings demonstrate that controlled lattice modification through Sc^{3+} incorporation allows for tuning structural and luminescent properties, offering a new approach for the design of advanced scintillators and luminescent materials with improved performance for targeted applications.

1. Introduction

Inorganic oxide single crystals represent one of the most important categories of functional materials, encompassing applications such as scintillation, phosphors, laser technologies, and optical sensors. Their prominence over other functional material groups is attributed to their favorable physicochemical properties, including non-hygroscopic nature, high chemical and radiation stability, mechanical hardness, excellent thermal stability, and well-established methodologies for bulk single-crystal growth.[1–7] The absence of phase transitions in aluminum garnets distinguishes them from many other materials, such as perovskites, which typically undergo structural changes at varying temperatures. This stability ensures that the material properties of aluminum garnets remain consistent across a broad temperature range. Consequently, the processes of crystal growth from the melt and the sintering of transparent ceramics are significantly simplified.[8,9] The invariance of the lattice structure during solidification eliminates phase changes, thereby producing materials that are free of cracks and exhibit excellent mechanical strength. This characteristic makes aluminum garnets particularly advantageous for applications requiring high reliability and durability. These inherent attributes contribute substantially to cost mitigation in the fabrication, operation, and maintenance of devices dedicated to the detection and analysis of ionizing radiation across diverse medical, and industrial applications. The Pr^{3+}-doped $Lu_3Al_5O_{12}$ (LuAG:Pr) single crystal deserves special consideration for radiation detection applications. Its physical and chemical merits, including a high density of 6.7 g cm^{-3}, a rapid scintillation decay time of 20 ns, and a theoretical light yield (LY) approaching 60 000 photons per MeV, synergistically contribute to its ability to provide high-resolution imaging and accurate counting measurements.[1] A notable advantage of Pr^{3+} ions in oxide garnets is their exceptional thermal sensitivity across a wide temperature range of 17–700 K.[7,10–14] These capabilities are of particular importance in high-energy physics experiments, medical imaging techniques such as positron emission tomography (PET), homeland security applications, radiation monitoring, and highly sensitive and accurate sensor systems.[7]

The growing demands for high resolution, efficiency, faster signal processing, and enhanced thermal sensitivity drive the imperative for further development of LuAG:Pr single crystals. A significant structural limitation of the $Lu_3Al_5O_{12}$ crystal lattice is the notably constrained ionic radius of Lu^{3+} ions (r_{VIII} = 0.997 Å; VIII – denotes the coordination number). This characteristic, combined with its high melting point exceeding 2100 K, serves as a driving force for ion displacement processes within the crystal lattice.[1,4,15] This process involves the displacement of Lu^{3+} ions from their preferred dodecahedral coordination to the octahedral coordination sites normally occupied by Al^{3+} ions, resulting in the formation of Lu_{Al}^{x} antisite defects.[1] These point defects act as electron trapping centers, significantly complicating the scintillation mechanism by quenching luminescence and slowing down the scintillation response. Consequently, the experimental light yield value was approximately 20 000 photons per MeV, accompanied by a slow component in the scintillation response over microsecond timescales.[16–18] Continuous efforts to enhance the scintillation properties of LuAG:Pr have involved compositional modifications by substituting Al atoms with Ga atoms. However, the incorporation of Ga has a detrimental effect, significantly lowering the energy barrier between the conduction band minimum and the $5d_1$ excited state of Pr^{3+} ions. This quenching effect has been demonstrated to inhibit the desired emission originating from the interconfigurational $4f^15d_1^1 \rightarrow 4f^2$ transition and progressively reduces the light yield

value.[7,19–21] However, a balanced substitution of Y for Lu atoms in Pr^{3+}-doped $(Lu,Y)_3Al_5O_{12}$ crystal resulted in a notable enhancement of the light yield by approximately 50%, accompanied by a significant acceleration of the slow component in the scintillation response.[11,13,22]

Lattice engineering through the manipulation of lattice parameters is a complex process that is constrained by a multitude of physicochemical factors. The incorporation of highly incompatible dopants, such as Pr^{3+} ions (r_{VIII} = 1.126 Å) into Lu^{3+} sites (r_{VIII} = 0.977 Å) with an ionic radius mismatch of approximately 15.28%,[14,15,23] can significantly increase the strain energy in the lattice around the incompatible dopant. This incompatibility reduces the solubility limit of incompatible atoms and deforms the polyhedral framework that constitutes the unit cell of the lattice.[14] Strain relaxation triggers a process of defect formation and local structural rearrangements within the host lattice, eventually leading to the formation of secondary phase inclusions.[14,24] The presence of structural defects and charge-trapping centers induces non-uniformities and compromises the functional performance of the material.[5,14,24,25] The correlation between cationic substitution, contraction and polyhedral expansion in the $RE_3M'_2M''_3O_{12}$ lattice underscores the existence of strong and intricate linkages within the garnet structure. The expansion of REO_8 dodecahedra induces compression of $M'O_6$ octahedra and $M''O_4$ tetrahedra.[26–28] This direct relationship between polyhedral deformation highlights the significance of meticulous lattice engineering in garnets by synergistically expanding dodecahedral, octahedral, and tetrahedral units.

This comprehensive study meticulously delves into the lattice engineering approach, particularly the simultaneous expansion of dodecahedral coordination (the site where the doping ion Pr^{3+} is incorporated) and octahedral coordination (where Sc substitutes for Al) and its impact on the microstructure, local structure rearrangement, lattice disorder degree, vibrational modes, luminescence, and scintillation properties and charged trap density. As a research model, a series of the Pr^{3+}-doped $Lu_{1.5}Y_{1.5}Al_{5-x}Sc_xO_{12}$ crystals, where x = 0.0, 0.5, 1.0, 1.5, 2.0, was used. This wide range of Sc atom concentrations enables the investigation of the effects of subtle expansion (for x equal to 0.5) to extreme expansion of the ScO_6 polyhedral framework, where local structure rearrangement initiates *via* the formation of secondary phase domains. The simultaneous expansion of dodecahedral and octahedral coordinations paves the way for incorporating higher concentrations of Pr^{3+} ions, reaching up to 0.15 at%.[14] Sc^{3+} ions not only expand the ScO_6 polyhedral framework but also induce locally perturbed potentials, leading to lattice distortions and the formation of localized states that facilitate electron–hole exchange interactions. These interactions promote the formation of bound e^-–h^+ states (excitons) around Sc^{3+} ions. The resonant energy state of these excitons with the $5d_1^1$ $4f^1$ energy state of Pr^{3+} ions enables energy transfer from the Sc^{3+}-bound excitons to Pr^{3+} ions.[29,30] This introduces an additional pathway for energy transfer from the lattice to Pr^{3+} ions, which can enhance their luminescence efficiency. The incorporation of Sc atoms into the host lattice significantly enhanced the degree of structural disorder, disrupting the local symmetry surrounding Pr^{3+} ions. This structure disorder led to a pronounced broadening of the excitation and emission bands, reflecting the altered local environment. Notably, this structural disorder resulted in a substantial enhancement of the luminescence intensity of Pr^{3+} ions. Consequently, Sc-admixed crystals exhibited enhanced emission intensity across a wide spectral range, encompassing the ultraviolet (UV), visible (VIS), and near-infrared (NIR) regions. To the best of our knowledge, this $Sc_{e^-\rightarrow h^+}{}^{3+} \rightarrow Pr^{3+}$ energy transfer mechanism was experimentally confirmed for the first time through excitation spectroscopy using synchrotron radiation. A key conclusion of this study was the identification of a Sc concentration threshold in the $Lu_{1.5}Y_{1.5}Al_{5-x}Sc_xO_{12}$ crystals, estimated at x = 1.5. At this critical concentration, the incorporation of Sc resulted in the formation of cubic bixbyite-like distorted perovskite inclusions within the garnet structure. This investigation further reveals that the atomic size mismatch between constituent ions introduces kinetic barriers that drive the co-precipitation of metastable phases. Significantly, the hypoeutectic crystal structure demonstrates a 16-fold enhancement in NIR emission intensity compared to single-phase crystal. These findings open new possibilities for the crystallization of hypoeutectic crystal compositions, offering valuable insights into the design of advanced photonic applications and optical devices, allowing for tailored emission characteristics based on specific spectral range requirements.

2. Methodology

2.1. Crystallization process

Single crystals were grown from the melt using the micro-pulling down (μ-PD) technique with radiofrequency (RF) inductive heating.[31,32] The starting materials were prepared by thoroughly mixing high-purity oxides of Lu_2O_3, Y_2O_3, Al_2O_3, Sc_2O_3, and Pr_6O_{11} (99.999% purity), obtained from Iwatani Corporation. The powdered mixture was melted under a flowing argon atmosphere *via* radio-frequency inductive heating within an iridium crucible. This crucible was specifically designed with five crystallization capillaries, each possessing a die diameter of 0.4 mm. Crystal growth was initiated using a LuAG seed oriented along the ⟨100⟩ crystallographic direction. The pulling rate during crystal growth was maintained at 0.05 mm min^{-1}.

2.2. Powder X-ray diffraction, SEM-EDS, and Raman spectroscopy

Powder X-ray diffraction (XRD). Small fragments of the grown crystals were pulverized into a fine powder using a mortar and pestle. Powder XRD analysis was carried out within the 2θ range of 15–70° using a D8 DISCOVER-HS (BRUKER) diffractometer. Cu-Kα radiation, with a wavelength (λ) and a photon energy (E) of approximately 8.05 keV, respectively, was employed for diffraction measurements.

Scanning electron microscopy (SEM) with energy-dispersive X-ray spectroscopy (EDS). The morphology and chemical composition of the Pr^{3+}-doped $(Lu,Y)_3(Al,Sc)_5O_{12}$ crystals series were

investigated using a field emission scanning Electron Microscope (FEI Nova NanoSEM 230), equipped with an Apollo X Silicon Drift Detector (SDD) and EDAX Genesis software. SEM images and EDS measurements were acquired at acceleration voltages of 5 and 30 kV, respectively. Due to the low concentration of Pr atoms in the crystals, EDS mapping and line profile intensity measurements were not feasible for aforementioned element and were not discussed in the paper. The surfaces of crystals were too rough to recorded high quality SEM images and EDS maps, therefore all measured samples were polished prior to scanning. In the first step, the crystals were included in the PolyFast (Struers) epoxy resin. In the following step, the specimens were subjected to mechanical polishing using SiC paper from 220 to 4000 grain (Struers) in order to remove deformation layers and obtain a flat surface for examination. After that, the prepared samples were coated with a thin layer of gold using an Auto 306 Coater with a Turbomolecular Pumping System (Edwards Vacuum) to enhance image contrast. Finally, obtained specimens were put under microscope and analysed by using secondary electron (SE) and dispersive X-ray signals (EDS) in order to obtain high quality SEM images and EDS maps, respectively.

Micro-Raman spectroscopy (μ-RS). Non-polarized Raman spectra were recorded at room temperature using a Renishaw InVia Raman microscope equipped with a thermoelectrically cooled (TE) CCD detector and an Ar^+ laser operating at a wavelength of 488 nm. Raman spectra were obtained within the 100–900 cm^{-1} spectral range, with a resolution better than 2 cm^{-1}. The laser beam, with a power below 5 mW, was focused onto the sample using a 50× objective. Raman peak positions were calibrated against a Si crystalline reference sample. Spectral band parameters, including peak center position, intensity, integral intensity, and FWHM (half-maximum width), were determined after baseline correction using the Wire 5.6 software fitting procedure.

High-spatial-resolution luminescence spectroscopy. High-spatial-resolution luminescence spectra were also recorded utilizing the Renishaw InVia Raman microscope. The excitation wavelength of 488 nm and optical objective with a magnification of 50× were employed. The laser beam power was set to 0.5 mW.

2.3. Optical, luminescence, scintillation, and thermoluminescence properties

Optical absorption, photoluminescence excitation, and emission spectra. The room-temperature absorption spectra of all crystals were measured across the 300–2000 nm spectral range using a double-beam UV-Vis-NIR spectrophotometer (Varian Cary 5000) with a spectral bandwidth set to 0.5 nm. To prevent distortions caused by moisture absorption in the NIR spectral range, the instrument was purged with high-purity Argon. The absorption range between 190–300 nm was measured using a Shimadzu 3101PC spectrophotometer. The photoluminescence excitation (PLE) and emission (PL) spectra were acquired using an Edinburgh Instruments FLS1000 spectrofluorometer. Both instruments were equipped with a xenon lamp excitation source, ensuring uniform excitation across the sample. To correct for instrumental artifacts, all recorded spectra underwent appropriate adjustments.

Time-resolved photoluminescence decay kinetics. Time-resolved photoluminescence (PL) decay kinetics were examined utilizing a pulsed nanoLED with a pulse duration of 0.2 ns and a repetition rate of 40 MHz. Temperature-dependent PL measurements were performed over a wide range (12–650 K) by employing a closed-cycle cryostat coupled to the FLS1000 spectrofluorometer. Prompt luminescence decay curves were obtained through time-correlated single photon counting. Decay curves were approximated with the following multiexponential function:

$$I(t) = \sum_i I_i e^{\frac{-t}{\tau_i}} + B \quad (1)$$

I represent the luminescence intensity, I_i denotes the intensity at 0 ns, t indicates the time, τ_i refers to the decay time, and B represents the background intensity. To quantify these parameters, the effective decay time ($\tau_{effective}$) was computed using the following formula:[33]

$$\tau_{effective} = \frac{\sum_i I_i \tau_i^2}{\sum_i I_i \tau_i} \quad (2)$$

here, I_i represents the intensity, and τ_i stands for the decay time value of the i-th component within the fit.

Synchrotron radiation measurements. Photoluminescence emission and excitation matrices (EEMs) were obtained under synchrotron radiation at the VUV time-resolved luminescence P66 beamline at the PETRA III storage ring of the Deutsches Elektronen-Synchrotron DESY (Hamburg, Germany). The excitation energy was set using a 2 m primary normal incidence McPherson monochromator within 0.8 nm resolution. The emission was analyzed using a 0.3 m Kymera 328i (Andor) spectrograph with the F/4.1 aperture and 0.4 nm spectral resolution. The detector was a thermoelectrically cooled CCD camera (Newton 920, BEX2-DD, Andor), and a set of high-pass Thorlabs filters was used to avoid the first and second orders in the data. The spectra were corrected both for the synchrotron radiation flux using the reference sodium salicilate excitation spectrum and for the sensitivity of the detection system using calibration curves produced within the previous measurements with Ocean Optics calibrated UV-VIS-NIR light source DH-2000. The automatic EEM scanning was performed using the home-made PyTango based software with a GUI, recently available at P66. The measurements at 8 K were performed using the Konti (Cryovac) liquid helium-cooled flow-type cryostat, under 1.0 × 10^{-9} mbar ultra-high vacuum conditions.

Radioluminescence (RL) and thermoluminescence (TL) studies. Radioluminescence (RL) spectra and thermoluminescence (TL) glow curves were obtained using an experimental setup comprising an Inel Cu-anode X-ray generator, an ARC SP-500i monochromator, a Hamamatsu R928 photomultiplier, and an APD Cryogenics helium cooler controlled by a Lake Shore 330 unit. TL measurements were performed between 10 and 300 K

at a heating rate of 0.14 K s^{-1}, following a 10-minute X-ray excitation. RL spectra were recorded starting at 350 K and terminating at 10 K, aiming to avoid potential contributions from the thermal release of charge carriers to the RL yield.

Scintillation light yield and decay time. Scintillation light yield and decay time were measured by enclosing the crystals in several layers of Teflon tape and optically coupling them to the light entrance window of an R7600 photomultiplier tube (PMT; Hamamatsu) using optical grease. The high voltage was provided by the ORTEC 556 power supply, and signals were extracted from the PMT anode. These signals then passed through a 2 and 10 μs shaping amplifier, the ORTEC 570, before being digitized by the Pocket MCA 8000A multi-channel analyzer (MCA; Amptek Co.). Scintillation decay curves were obtained using a digital oscilloscope (Tektronix TDS3034B) under excitation by 622 keV photons from the 137Cs radioisotope.

2.4. Electron paramagnetic resonance (EPR)

Electron paramagnetic resonance (EPR) measurements were conducted on a commercial Bruker EMXplus spectrometer operating at the X band (9.4 GHz) and TE011 mode. The measurements were performed at 20 K using an Oxford Instruments ESR900 cryostat. The crystal was placed in a quartz tube for the measurements. X-ray irradiation of samples in the quartz tube was conducted at 20 K using ISO-DEBYEFLEX 3003 highly stabilized X-ray equipment for structural analysis (tungsten X-ray tube, 50 kV, 30 mA). The majority of graphical visualizations were generated utilizing Veusz, an open-source scientific plotting software developed by Sanders.[34]

3. Experimental results and interpretation

3.1. Powder X-ray diffraction, SEM-EDS, and Raman spectroscopy

Fig. 1a depicts as-grown crystal rods alongside polished radial plates of Pr^{3+}-doped $Lu_{1.5}Y_{1.5}Al_{5-x}Sc_xO_{12}$, where x = 0.0, 0.5, 1.0, 1.5, and 2.0. All examined crystals exhibit a crack-free and regular cylindrical morphology. The crystals with scandium concentration up to x = 1.5 demonstrate good optical transparency. However, the Pr^{3+}-doped $Lu_{1.5}Y_{1.5}Al_3Sc_2O_{12}$ crystal (x = 2.0) exhibits significantly reduced transparency. Cross-sectional microscopic analysis of the Pr^{3+}-doped $Lu_{1.5}Y_{1.5}Al_3Sc_2O_{12}$ crystal reveals a systematic reduction in optical transparency throughout the entire sample area. This transparency degradation indicates the formation of compositionally heterogeneous inclusions within the crystal lattice, which scatter the incident light.

The powder X-ray diffraction patterns depicted in Fig. 1b correspond to Pr^{3+}-doped $Lu_{1.5}Y_{1.5}Al_{5-x}Sc_xO_{12}$ crystals with

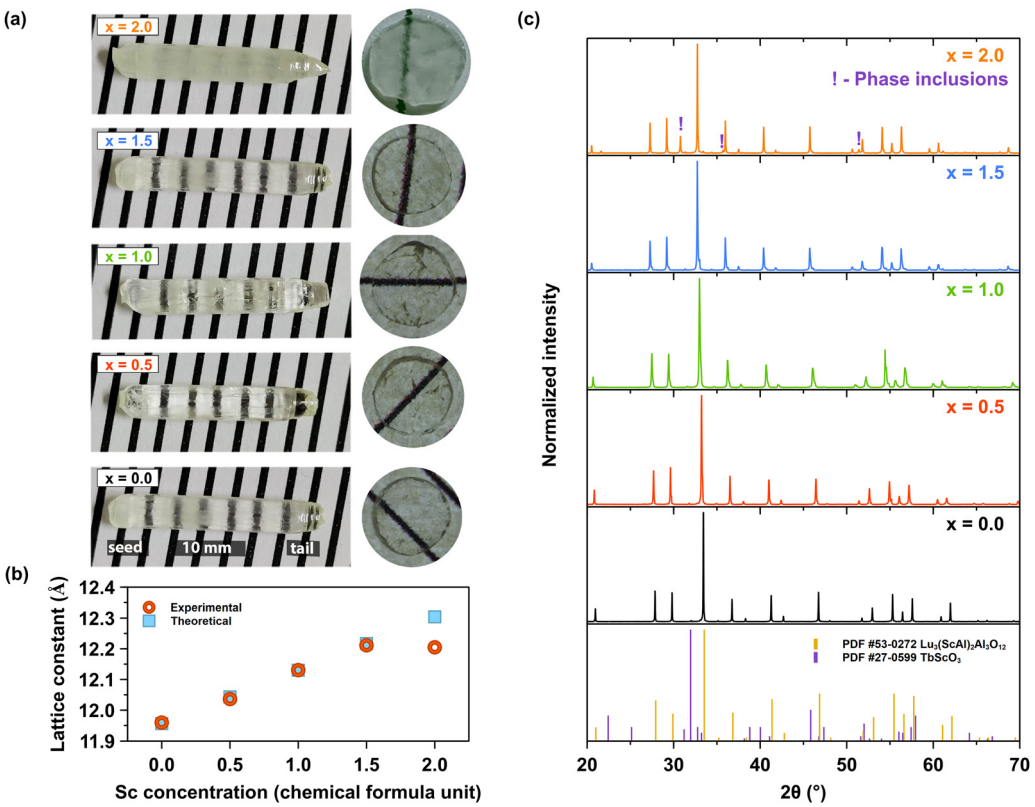

Fig. 1 (a) As-grown crystal rods of Pr^{3+}-doped $Lu_{1.5}Y_{1.5}Al_{5-x}Sc_xO_{12}$, where x = 0.0, 0.5, 1.0, 1.5, 2.0 along with polished radial plates cut from the central part of the crystal, (b) theoretical (PDF #53-0272, $Lu_3(AlSc)_2Al_3O_{12}$) and experimentally recorded PXRD patterns for Pr^{3+}-doped $Lu_{1.5}Y_{1.5}Al_{5-x}Sc_xO_{12}$ crystals with increasing Sc^{3+} ions concentration, (c) experimentally determined lattice constant a_0 as a function of Sc^{3+} ions concentration compared with theoretical values.

varying concentrations of Sc^{3+} ions. As the substitution of the Sc atoms for Al proceeds, the crystalline structure maintains its garnet-type phase. The PXRD data confirms that all samples crystallize in the cubic space group $Ia\bar{3}d$ (No. 230) of the garnet crystal system. The exception arises in the case of the Pr^{3+}-doped $Lu_{1.5}Y_{1.5}Al_3Sc_2O_{12}$ crystal (x = 2), wherein additional diffraction peaks are observed (see Fig. 1b). These additional peaks are attributed to the presence of perovskite phase inclusions within the dominant garnet lattice. The presence of perovskite phase inclusions in Pr^{3+}-doped $Lu_{1.5}Y_{1.5}Al_3Sc_2O_{12}$ crystals (x = 2.0) is a significant factor contributing to the observed reduction in transparency. Fig. 1c presents an analysis between the experimentally estimated and theoretically calculated lattice constants a_0 as a function of increasing Sc^{3+} ions concentration in Pr^{3+}-doped $Lu_{1.5}Y_{1.5}Al_{5-x}Sc_xO_{12}$ crystals. The expansion of the host lattice constants correlates well with the calculated values for Sc concentrations up to x = 1.5. Specifically, the lattice constants expand from 11.9594 Å to 12.2114 Å for the Pr^{3+}-doped $Lu_{1.5}Y_{1.5}Al_5O_{12}$ (x = 0.0) and $Lu_{1.5}Y_{1.5}Al_{3.5}Sc_{1.5}O_{12}$ (x = 1.5) crystals, respectively. However, marginal decrease in the lattice constant is observed for the Pr^{3+}-doped $Lu_{1.5}Y_{1.5}Al_3Sc_2O_{12}$ crystal (x = 2.0), indicating a reversal in the expansion trend. This observation aligns with the experimental PXRD patterns and substantiates that at higher concentrations of the larger Sc^{3+} cations, there is a decreased propensity for these cations to substitute for Al sites in octahedral coordination. Consequently, it becomes energetically more favorable for the Sc elements to form secondary perovskite phase inclusions rather than integrating into the octahedral sites. This behavior elucidates the noted deviation from Vegard's law observed in the experimental data.[35] Deviations from Vegard's law are well-documented, often attributed to factors such as disparities in component sizes and structural incompatibilities.[14,35] The observed effect provides compelling evidence regarding the inherent constraints associated with the incorporation of solute species into a solid matrix when the atomic radii of the solute and solvent atoms exhibit significant mismatch.[4,14,28] The experimental results reveal a compositional threshold for the saturation of Sc^{3+} ions in the octahedral sites of Pr^{3+}-doped $Lu_{1.5}Y_{1.5}Al_{5-x}Sc_xO_{12}$ occurring at x = 1.5. This assertion is corroborated by the substantial deviation between the experimentally estimated lattice constant a_0 (12.2049 Å), and the theoretically predicted value for complete saturation (12.3041 Å) in the Pr^{3+}-doped $Lu_{1.5}Y_{1.5}Al_3Sc_2O_{12}$ crystal (x = 2.0). This observation implies an incomplete incorporation of Sc^{3+} cations into the octahedral sites of the Pr^{3+}-doped $Lu_{1.5}Y_{1.5}Al_{5-x}Sc_xO_{12}$ crystal when x = 2.0. Consequently, the residual Sc atoms that exceed the substitutional capacity of the octahedral sites precipitate out, leading to the formation of perovskite phase inclusions within the garnet structure.

The EDS analysis serves as an imaging tool to visualize the distribution of atoms within a crystal structure. Fig. 2 and 3 present the EDS maps and corresponding line profiles for the Lu, Y, Al, Sc, and O elements, respectively. The EDS analysis revealed radial variations in the elemental distributions, exhibiting distinct patterns that depended on the concentration of Sc elements. The elemental variability observed in the crystallization volume is notable for its localized, point-like regions, primarily concentrated in areas where the molten material was

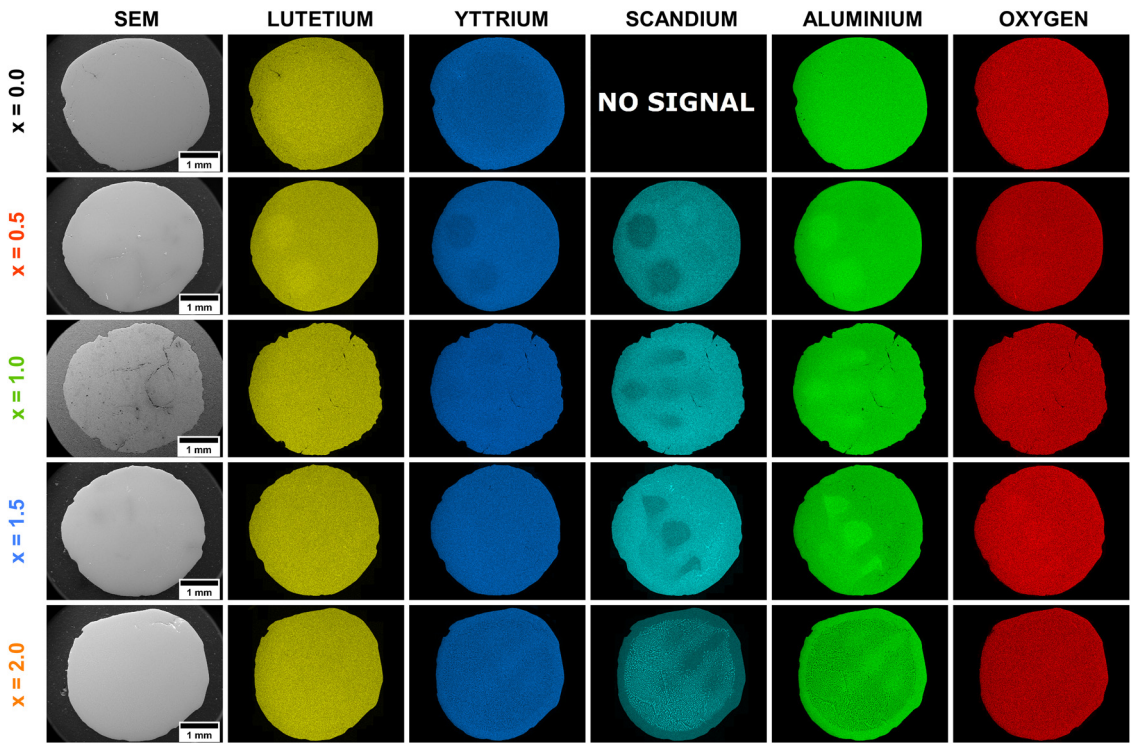

Fig. 2 The multi-elemental EDS maps illustrating the spatial distribution of Lu (yellow), Y (blue), Sc (cyan), Al (green) and O (red) within Pr^{3+}-doped $Lu_{1.5}Y_{1.5}Al_{5-x}Sc_xO_{12}$ crystals with increasing Sc^{3+} ions concentration.

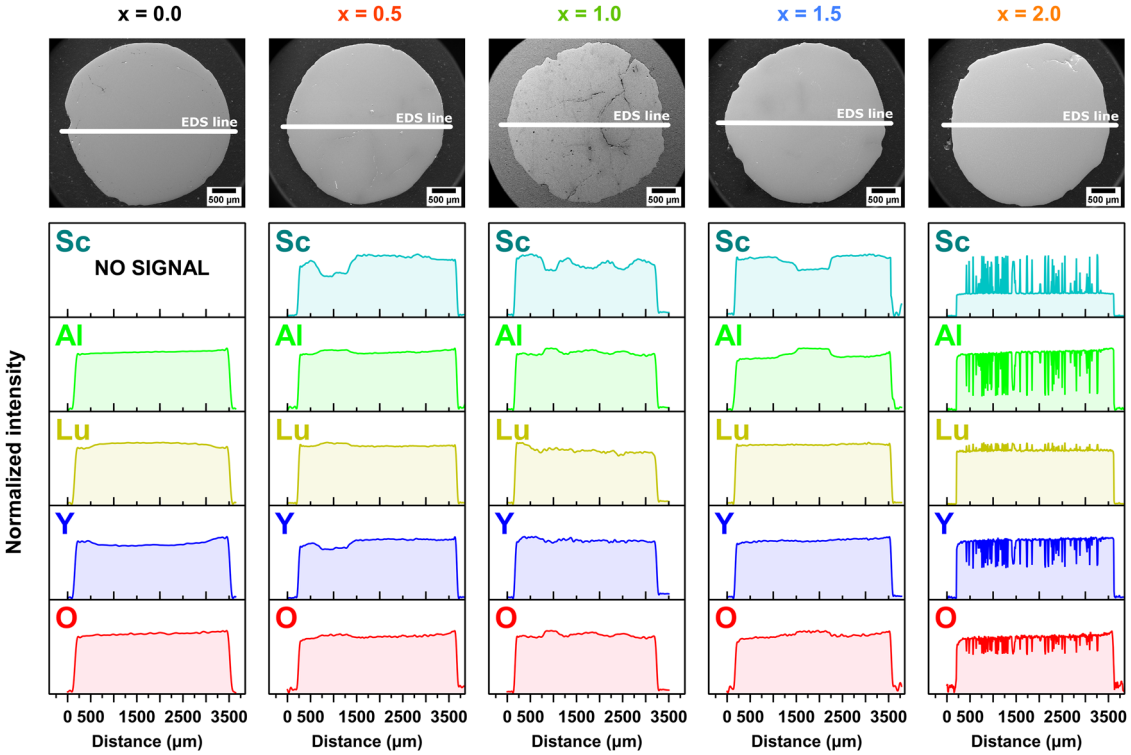

Fig. 3 EDS radial distribution profiles illustrating the spatial distribution of Sc (cyan), Al (green), Lu (yellow), Y (blue) and O (red) atoms in the Pr^{3+}-doped $Lu_{1.5}Y_{1.5}Al_{5-x}Sc_xO_{12}$ crystals with increasing Sc^{3+} ions concentration.

ejected through the crystallization capillary. These point-like regions form rounded spots embedded within the main crystal structure. The brighter regions of these spots reflect higher concentrations of certain elements, while the darker regions correlate with lower concentrations of the examined atoms. Additionally, the enrichment of one element within a spot is associated with the concomitant depletion of another element. An illustrative example is the Pr^{3+}-doped $Lu_{1.5}Y_{1.5}Al_{3.5}Sc_{1.5}O_{12}$ crystal (x = 1.5). In this case, Al elements show enrichment within the rounded spots, indicated by a brighter green color. Conversely, these areas are depleted in Sc atoms, which are represented by a darker cyan color. This pattern highlights the elemental segregation and the intricate interplay between atomic size mismatch and concentrations in the crystal lattice.

It is noteworthy that although the crucible used for crystal growth featured five crystallization capillaries, the EDS maps do not display all five regions with distinct chemical compositions. Furthermore, it has been demonstrated that the number of heterogeneous spots observed in the EDS maps is subject to variation following the Sc^{3+} ions concentration. This suggests that the molten material was not uniformly ejected from the five capillaries, resulting in compositional differences in the melt ejected from each capillary. If the segregation effect, attributed to the mismatch in ionic radii, were to occur uniformly at the liquid/solid interface, all capillaries would exhibit the same or similar behavior. Specifically, at the liquid/solid interface of each capillary, the same segregation mechanism would manifest, enriching the rim and core with larger ions and with smaller ions, respectively. However, the observed variations in chemical composition and the number of heterogeneous spots imply non-uniform ejection dynamics, indicating that factors beyond ionic radius mismatch may influence the segregation process during crystallization. However, it should be noted that this effect is only observed when the melt contains an incompatible element, *i.e.* Sc. The observation that the $Lu_{1.5}Y_{1.5}Al_5O_{12}$ crystal, which does not contain Sc, exhibits better homogeneity, lends support to the conclusion. In this sample, the typical behavior of elemental distribution is observed, where ions with larger ionic radii, such as Y^{3+} ions, show enrichment at the crystal rim and depletion at the crystal center. Conversely, Lu^{3+} ions, having a smaller ionic radius, exhibit the opposite behavior, with depletion at the crystal rim and enrichment in the central regions.[5]

The exception to this pattern is observed in the Pr^{3+}-doped $Lu_{1.5}Y_{1.5}Al_{3.0}Sc_{2.0}O_{12}$ sample (x = 2.0), where the crystal volume, excluding the rim, exhibits the hypoeutectic composition. The secondary phase inclusions display a triangular morphology, with each triangle enriched in Sc and Lu elements. This observation aligns with the PXRD results (see Fig. 1b), which indicate that the triangles predominantly form a perovskite structure, while Al, Y and O elements develop a garnet phase. Furthermore, the formation of this hypoeutectic structure also explains the observed deviation from Vegard's law. For the Pr^{3+}-doped $Lu_{1.5}Y_{1.5}Al_{5-x}Sc_xO_{12}$ crystals where $x > 1.5$, it is thermodynamically more favorable for Sc ions to form perovskite phase inclusions rather than incorporating into octahedral coordination within the garnet phase. This mechanism occurs when the concentration of large, incompatible atoms reaches the solubility threshold.[4,14,24,36–39]

The EDS line profiles provide comprehensive insights into the changes in elemental distribution imposed by Sc admixing. Notably, the EDS line profiles reveal that the smaller Lu elements enrich the central regions, while the larger yttrium Y elements are concentrated at the rim within the $Lu_{1.5}Y_{1.5}Al_5O_{12}$ crystal. In crystals admixed with Sc elements, the areas depleted in Sc (exhibiting lower intensity) and concurrently enriched in Al (higher intensity) are primarily concentrated in areas where the molten material was ejected through the crucible capillary. Furthermore, this observation confirms that the melt ejected from each capillary differed in composition. Interestingly, within these rounded spots, the Lu and Y elements follow the same trend, with the larger Y elements accumulating at the rim of the rounded spot and the smaller Lu elements concentrating within the central part. The spatial distribution analysis reveals a systematic segregation pattern of heterogeneous elements ejected from each capillary: elements with larger atomic radii predominantly migrate toward the peripheral regions of the capillary, whereas elements with smaller atomic radii exhibit preferential concentration within the central domains. This suggests that the crystallization process occurs independently within each capillary.[24,40] Another important conclusion is that the melt in the crucible is heterogeneous. Furthermore, the implementation of a 0.1 mm diameter capillary effectively inhibits atomic back-diffusion from the liquid/crystal interface to the crucible reservoir, thereby promoting heterogeneous crystallization processes. This geometric constraint significantly influences the crystallization kinetics and resultant phase formation. The EDS line profile for the Pr^{3+}-doped $Lu_{1.5}Y_{1.5}Al_{3.0}Sc_{2.0}O_{12}$ crystal (x = 2.0) demonstrates eutectic perovskite-garnet composite structure. The spatial distribution of elements ejected from each capillary demonstrates a spontaneous self-organizing phenomenon, wherein size-dependent elemental segregation occurs as an intrinsic mechanism during the crystallization process, suggesting a thermodynamically driven ordering behavior. This localized crystallization phenomenon represents a significant advancement in hypoeutectic materials engineering, enabling enhanced control over phase self-organization and microstructural evolution. This novel approach enables optimal spatial organization of both phases, leading to materials that display enhanced structural integrity and functional properties. The methodology shows significant promise for the design of next-generation composite materials, allowing for the precise control of microstructures and the customization of performance characteristics to meet specific application demands. To elucidate the impact of Sc incorporation on host lattice disorder and characterize the structural properties of secondary phase inclusions, detailed vibrational spectroscopy analyses were conducted.

The symmetry of Pr^{3+}-doped $Lu_{1.5}Y_{1.5}Al_{5-x}Sc_xO_{12}$ crystals is described by the cubic $Ia\bar{3}d$ space group. The group theory for such a structure predicts 240 normal vibration modes in the vicinity of the Brillouin zone center:[41]

$$\Gamma = 3A_{1g} + 5A_{2g} + 8E_g + 14F_{1g} + 5A_{1u} + 5A_{2u} + 10E_u + 18F_{1u} + 16F_{2u} \quad (3)$$

Among them 17 ungerade modes are infrared active ($17F_{1u}$), 55 are optically inactive, and 25 gerade modes ($3A_{1g}$ + $8E_g$ + $14F_{2g}$) are active in Raman spectroscopy. This theoretical prediction should be considered only as a limit since the observation of modes is often hindered by their accidental degeneracy, weak intensity, or electron transitions.[42–44] Generally, the $RE_3M'_2M''_3O_{12}$ garnet Raman response is dominated by $M''O_4$ tetrahedra-related bands. It can be divided into two main regions: (i) low energy one below 500 cm^{-1}, containing RE ions translations, alongside translational, librational, and internal antisymmetric stretching vibrations (ν_3) of $M'O_4$ tetrahedra, and (ii) high energy range from 500 to roughly 900 cm^{-1}, with breathing (ν_1), quadrupolar-like (ν_2), and deformations (ν_4) of $M'O_4$ units. In an ideal case, all oxygens forming $M''O_6$ octahedra are equally spaced from the inner M atom, and vibrations of such structure described by the O_h point group are Raman inactive.

The obtained room temperature and unpolarized Raman spectra are included in Fig. 4a. The positions of modes with assigned symmetries and vibration types are summarized in Table S1 in ESI.† In total, 16, 15, 14, 14, and 14 bands were collected for the Pr^{3+}-doped $Lu_{1.5}Y_{1.5}Al_{5-x}Sc_xO_{12}$ crystals, where x = 0.0, 0.5, 1.0, 1.5 and 2.0, respectively. For the Pr^{3+}-doped $Lu_{1.5}Y_{1.5}Al_5O_{12}$ crystal (x = 0.0), the four most intensive peaks located at 260 (F_{2g}), 374 (A_{1g}), 398 (E_g), and 790 cm^{-1} (F_{2g}). These and most of the other observed bands are separated and relatively narrow, with FWHM below 16 cm^{-1}. The latter indicates a well-developed ordered crystal structure. The overall spectrum resembles that of isomorphous YAG, which, due to its thorough examination by Raman and computational methods, serves as the main reference for interpretation.[44–47] With increasing Sc^{3+} ions concentration in the YAG crystal structure, the A_{1g} and E_g modes become visible in the spectra as a single, greater peak. This accidental degeneracy can be corroborated by considering the height ratio of the resultant and the other two strong F_{2g} modes. The ratio exhibits a positive gradient in the interval $0.5 \leq x \leq 1.5$, indicating enhanced overlap, followed by a notable decline within the range $1.5 < x \leq 2.0$ (as illustrated in the upper panels of Fig. 4a). This observation may suggest that the A_{1g} and E_g modes have exchanged their order, resulting in the E_g mode being positioned at a lower energy level. The spectral deconvolution of the region spanning 280–440 cm^{-1}, which incorporates the two subsidiary E_g and F_{2g} modes, is depicted by dashed black lines in Fig. 4a. A notable consequence of elevated Sc^{3+} ions concentration is the manifestation of unexpected broad spectral features within the 570–770 cm^{-1} spectral region, particularly pronounced in the Pr^{3+}-doped $Lu_{1.5}Y_{1.5}Al_{5-x}Sc_xO_{12}$ crystals, where x = 0.5 and 2.0. The underlying mechanism responsible for these spectral features remains not fully understood. It is possible to propose two potential explanations for this phenomenon. Firstly, in the Pr^{3+}-doped $Lu_{1.5}Y_{1.5}Al_{4.5}Sc_{0.5}O_{12}$ (x = 0.5) and $Lu_{1.5}Y_{1.5}Al_3Sc_{2.0}O_{12}$ (x = 2.0) crystals, it is conceivable that certain electronic levels of the Pr^{3+} ions may manifest in this region as a consequence of crystal field splitting. Secondly, these features might arise from structural distortions within the ScO_6 octahedra.

The reduction in structural symmetry induces significant modifications in the vibrational spectrum, manifesting as the activation of previously IR-active and silent modes in the Raman spectra. The spectral evolution, illustrated in Fig. 4b, reveals distinctive peak position shifts across the compositional range. The magnitude of these shifts, denoted by Δ, represents the difference between the extrema values estimated for Pr^{3+}-doped $Lu_{1.5}Y_{1.5}Al_{5-x}Sc_xO_{12}$ crystals, where x = 0.0 and 2.0, respectively. A predominant redshift tendency is observed for the majority of vibrational modes, with shifts typically spanning several wavenumbers (cm^{-1}). Notable exceptions to this trend are observed in the A_{1g} and E_g symmetry modes, centered at approximately 375 and 535 cm^{-1}, respectively. While the primary mechanism underlying these spectral modifications can be attributed to the expansion of the lattice parameter, whereby increased interatomic distances generally correlate with decreased vibrational energies (Fig. 1c), the observed peak shifts cannot be fully rationalized by the experimentally determined lattice parameters of the Pr^{3+}-doped $Lu_{1.5}Y_{1.5}Al_3Sc_{2.0}O_{12}$ (x = 2.0) crystal. This discrepancy suggests that additional structural factors, specifically alterations in the internal bond lengths and angular distortions of the AlO_4 or ScO_4 tetrahedral units, contribute significantly to the observed spectral evolution.

A comprehensive analysis of the crystalline structural quality was conducted through examination of the FWHM parameters for the most prominent Raman bands, as depicted in Fig. 4c. The FWHM exhibits a systematic increase of several wavenumbers across the compositional range from x = 0.0 to x = 1.0, with the Pr^{3+}-doped $Lu_{1.5}Y_{1.5}Al_5O_{12}$ crystal demonstrating excellent structural order. This observation aligns with theoretical predictions, as the absence of Sc^{3+} ions ensures enhanced crystallographic periodicity and minimizes local structural distortions

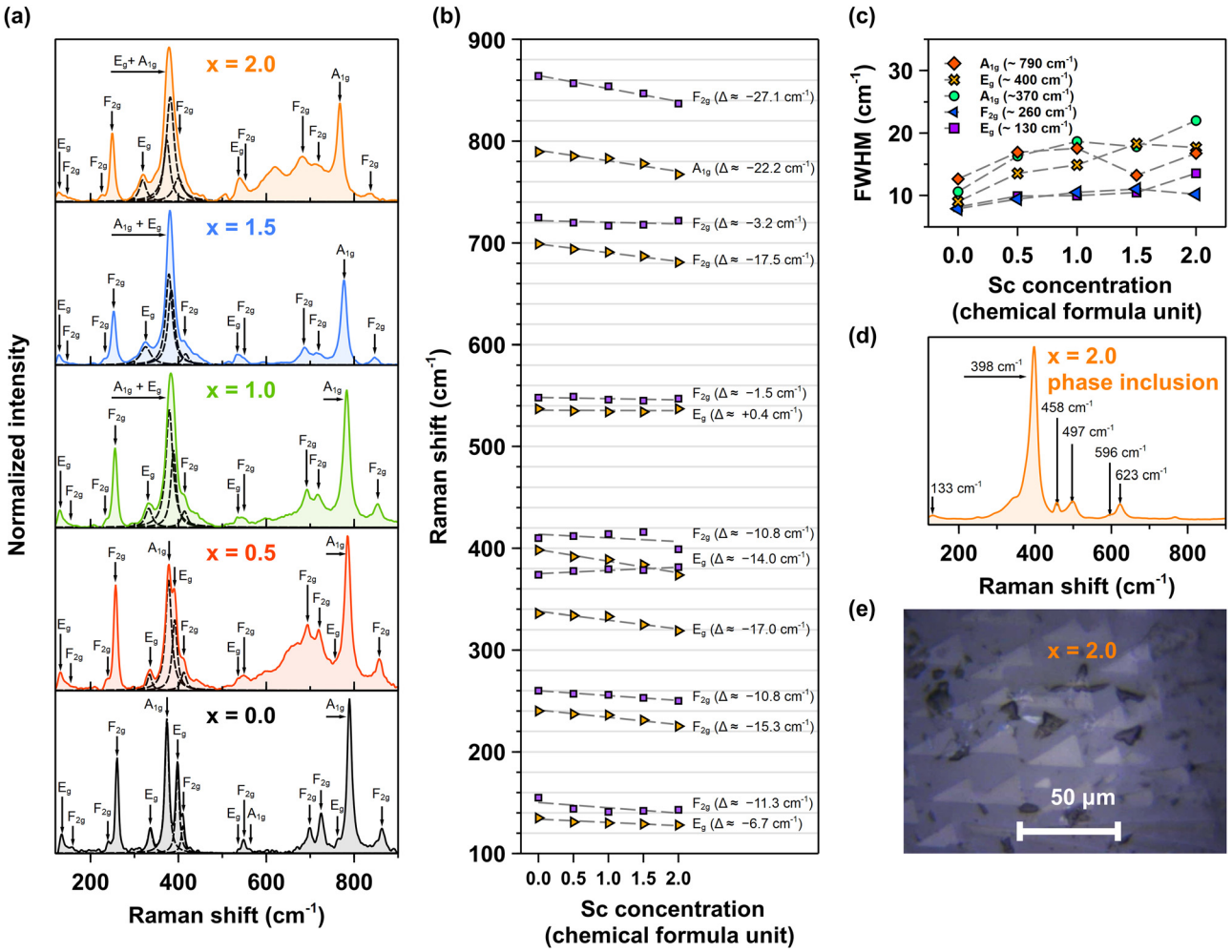

Fig. 4 (a) Room-temperature, unpolarized Raman spectra of Pr^{3+}-doped $Lu_{1.5}Y_{1.5}Al_{5-x}Sc_xO_{12}$ crystals with increasing Sc^{3+} ions concentration. Dashed lines show the deconvolution of bands within the 300–450 cm^{-1} spectral range, (b) positions of selected Raman bands as a function of Sc^{3+} ions concentration. The differences between the Pr^{3+}-doped $Lu_{1.5}Y_{1.5}Al_{5.0}O_{12}$ (x = 0.0) and $Lu_{1.5}Y_{1.5}Al_{3.0}Sc_{2.0}O_{12}$ (x = 2.0) crystals are indicated in parentheses on the right; a negative value signifies that the band for the $Lu_{1.5}Y_{1.5}Al_{3.0}Sc_{2.0}O_{12}$ crystal is shifted to lower energy relative to the $Lu_{1.5}Y_{1.5}Al_{5.0}O_{12}$ crystal, (c) FWHM of selected Raman bands as a function of Sc^{3+} ions concentration, (d) room-temperature, unpolarized Raman spectrum of secondary phase inclusion within the main $Lu_{1.5}Y_{1.5}Al_3Sc_2O_{12}$ garnet phase, (e) optical image of example phase inclusions (bright triangles) acquired at a magnification of 50×.

that would otherwise arise from the larger ionic radius of Sc^{3+} ions. The correlation between Sc^{3+} ions concentration and peak broadening offers compelling evidence for the influence of ionic size effects on the increased disorder within the host lattice. For the Pr^{3+}-doped $Lu_{1.5}Y_{1.5}Al_{5-x}Sc_xO_{12}$ crystals, where $x = 1.5$ and 2.0, the observed trend becomes less clear, as some bands exhibit a decrease in width. This phenomenon may suggest that the Sc : Al ratio equal to 1 : 4 leads to saturation of the garnet lattice disorder. The behavior is likely influenced by a combination of factors, such as selective distortions of specific symmetrical units and the activation of modes resulting from reduced symmetry. However, a thorough analysis of these complexities would require theoretical calculations for validation. Additionally, the presence of phase inclusions in the Pr^{3+}-doped $Lu_{1.5}Y_{1.5}Al_{3.0}Sc_{2.0}O_{12}$ (x = 2.0) crystal, may also contribute to the modifications observed in the vibrational characteristics.

To investigate the nature of the perovskite phase present in the Pr^{3+}-doped $Lu_{1.5}Y_{1.5}Al_3Sc_2O_{12}$ crystal, spectra from these specific regions were recorded, as illustrated in Fig. 4d and e. An optical image demonstrating the phases reveals a repetitive triangular morphology, as shown in Fig. 4e. The vibrational spectra obtained from these regions display fundamentally different characteristics from those of the primary garnet phase, indicating a distinct crystallographic structure. A comprehensive comparison with the existing literature[48–52] enabled the identification of the structure as a cubic bixbyite-like distorted perovskite, characterized by the space group $Ia\bar{3}$. The main characteristic proving such assignment is the strong, degenerate band consisting of two modes of A_g and F_g symmetry located at about 398 cm^{-1}. The chemical composition of the inclusions is presumably $Lu_{1-y}Y_yScO_3$ with $y < 1 - y$ the lack of aluminum and yttrium can be proven by its deficiencies visible in the EDS maps (see Fig. 2 and 3) and also by employing the Goldschmidt tolerance factor[53] defined as:

$$t = \frac{r_A + r_O}{\sqrt{2}(r_B + r_O)} \quad (4)$$

For $LuScO_3$ and $YScO_3$ the parameter roughly equals 0.80, and 0.82, respectively, assuming Lu^{3+}(IX), Y^{3+}(IX), Sc^{3+}(VI), and O^{-2}(VI) oxidation states.[15] These fall well within $0.78 < t < 0.83$ range appropriate for cubic, bixbyite-like structures.[52] On the other hand, $YAlO_3$ and $LuAlO_3$ take values of 0.90, and 0.89, suggesting an orthorhombic crystal system.[54] Indeed, such perovskites are well known to crystalize in *Pbnm* space group and give Raman bands distinctive from those in Fig. 4d.[43,55,56] The identification of the bixbyite phase presents significant implications for the structural and physical properties of Pr^{3+}-doped $Lu_{1.5}Y_{1.5}Al_3Sc_2O_{12}$, contributing to notable structural coherence within the crystal. The presence of this phase, specifically the $Lu_{1-y}Y_yScO_3$ structure with its characteristically smaller lattice parameter, provides a plausible explanation for the observed deviation from Vegard's law.[51,57] In addition, a local change in the environment of Pr^{3+} ions can affect their electronic transitions. The ordering of Sc^{3+}, Lu^{3+}, and O^{2-} ions in deformed perovskite phases may also cause their deficiencies in the rest of the material, leading to an increased number of vacancies and explaining the lower optical quality of the Pr^{3+}-doped $Lu_{1.5}Y_{1.5}Al_3Sc_{2.0}O_{12}$ (x = 2.0) crystal in comparison to the other crystals in the series, as evidenced by the broadened Raman bands. The detailed characterization of bixbyite inclusions and their impact on the $Lu_{1.5}Y_{1.5}Al_3Sc_2O_{12}$ garnet structure necessitates further investigation. Given the substantial volume of experimental data required and the complexity of this phenomenon, a comprehensive analysis will be presented in subsequent work dedicated exclusively to elucidating these phase relationships.

3.2. Temperature, time, and spatial dependence of Pr^{3+} photoluminescence properties

The room-temperature photoluminescence excitation spectra for Pr^{3+} emission are systematically investigated in $Lu_{1.5}Y_{1.5}Al_{5-x}Sc_xO_{12}$ crystals where x ranging from 0.0 to 2.0, with emission monitored at 340 nm corresponding to the interconfigurational $4f^15d_1^1 \rightarrow 4f^2$ transitions (see Fig. 5a). The excitation spectra reveal two primary interconfigurational transitions: the $4f^2 \rightarrow 5d_2^1 4f^1$ transition centered at 240 nm and the $4f^2 \rightarrow 5d_1^1 4f^1$ transition centered at 285 nm.[14] Notably, Sc admixing induces significant broadening of these excitation bands. This spectral broadening can be attributed to the increased lattice disorder induced by Sc incorporation. The Sc admixing leads to a higher concentration of Pr^{3+} ions that experience varied local environments, resulting in reduced symmetry. This phenomenon is corroborated by the vibrational spectra, which reveal distinct variations indicative of these effects.[14] A particularly important observation is the appearance of an additional excitation band centered initially at 200 nm in the Pr^{3+}-doped $Lu_{1.5}Y_{1.5}Al_{4.5}Sc_{0.5}O_{12}$ (x = 0.5) crystal, which progressively shifts to 205 nm for the Pr^{3+}-doped $Lu_{1.5}Y_{1.5}Al_3Sc_{2.0}O_{12}$ (x = 2.0) crystal. This band originates from electron–hole (e^+–h^-) pairs bound to Sc^{3+} ions, termed a bounded exciton. Remarkably, the intensity of this excitonic band demonstrates a linear increase with Sc^{3+} ions concentration, reaching peak intensity in the crystal with x = 2.0 which is approximately twice that observed in the Pr^{3+}-doped $Lu_{1.5}Y_{1.5}Al_{4.5}Sc_{0.5}O_{12}$ (x = 0.5) crystal. The systematic appearance and intensity progression of the excitonic band provide evidence for an efficient excitation energy transfer mechanism from excitons bound to Sc^{3+} ions to Pr^{3+} ions.[29,30]

Fig. 5b compares the room-temperature photoluminescence spectra of Pr^{3+} emissions, excited *via* the interconfigurational $4f^2 \rightarrow 5d_2^1 4f^1$ transition at 240 nm in $Lu_{1.5}Y_{1.5}Al_{5-x}Sc_xO_{12}$ crystals. The emission spectra demonstrate two distinct spectral regions: a dominant interconfigurational $4f^15d_1^1 \rightarrow 4f^2$ broadband emission spanning 285–450 nm and sharp emission lines between 470–700 nm originating from the intraconfigurational $4f^2 \rightarrow 4f^2$ transitions of Pr^{3+} ions. The Sc admixing induces significant modifications to both spectral features. The interconfigurational $4f^15d_1^1 \rightarrow 4f^2$ broadband demonstrates progressive broadening, while the intensity of the intraconfigurational $4f^2 \rightarrow 4f^2$ sharp lines exhibits a systematic increase with rising Sc^{3+} ions concentration. These observations align with the excitation spectra and provide further evidence that Sc admixture

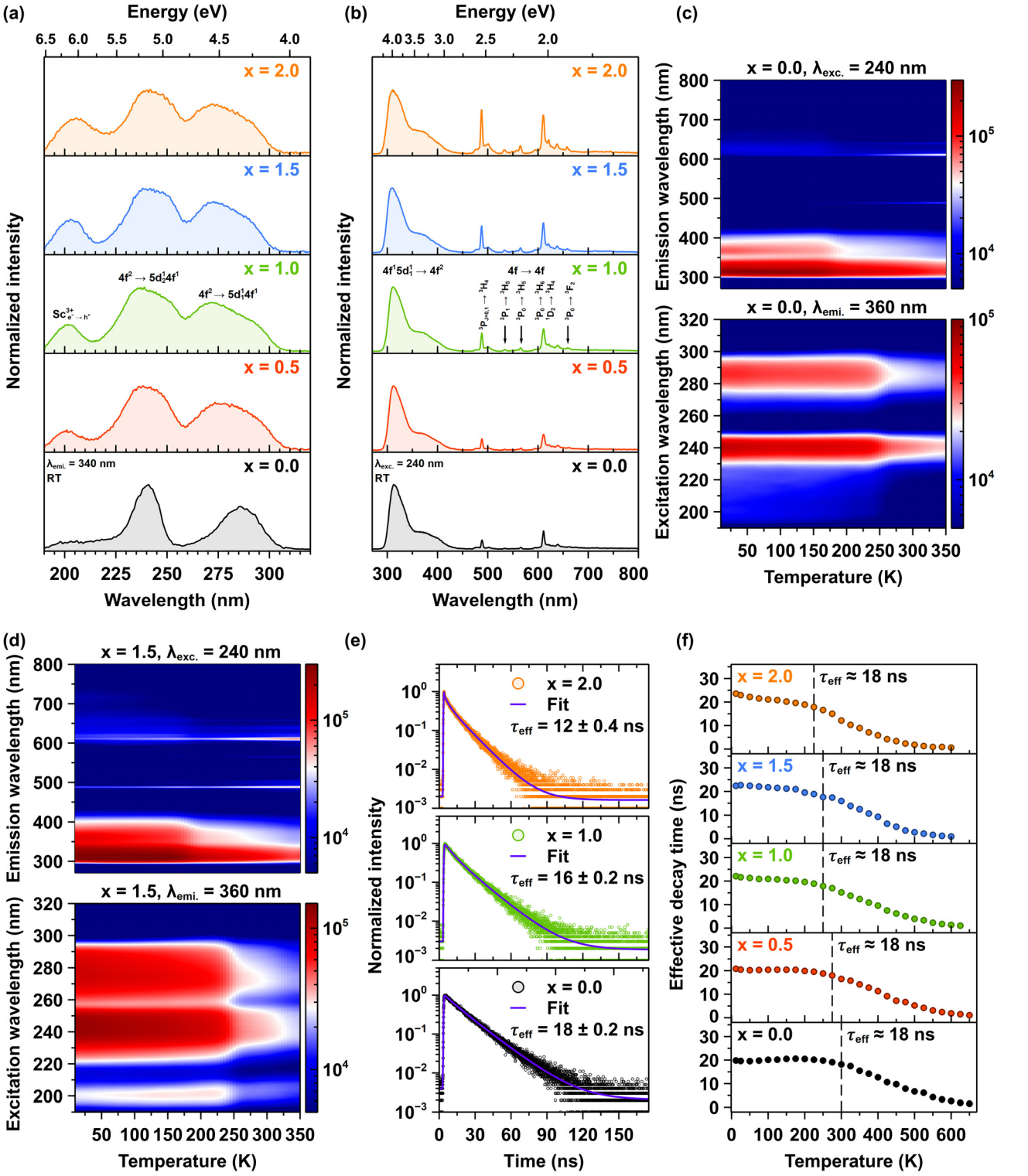

Fig. 5 (a) Room-temperature excitation spectra of Pr^{3+} ions for the $4f^15d_1^1 \rightarrow 4f^2$ transition at 360 nm, and (b) corresponding emission spectra excited at 240 nm. (c) 2D temperature-dependent (10–340 K) maps of photoluminescence emission (upper panel, λ_{exc} = 240 nm) and excitation spectra (lower panel, λ_{emi} = 360 nm) for the Pr^{3+}-doped $Lu_{1.5}Y_{1.5}Al_5O_{12}$ (x = 0.0) and (d) $Lu_{1.5}Y_{1.5}Al_{3.5}Sc_{1.5}O_{12}$ (x = 1.5) crystals (e) RT photoluminescence decay times of Pr^{3+} ions (λ_{exc} = 280 nm, λ_{emi} = 320 nm) in the Pr^{3+}-doped $Lu_{1.5}Y_{1.5}Al_{5-x}Sc_xO_{12}$ crystals, where x = 0.0, 1.0, and 2.0. (f) Temperature-dependent decay kinetics of the Pr^{3+} emission at 320 nm under 280 nm excitation in $Lu_{1.5}Y_{1.5}Al_{5-x}Sc_xO_{12}$ crystals, where x = 0.0, 0.5, 1.0, 1.5, 2.0.

introduces significant disorder into the host lattice. This disorder effectively lowers the symmetry around the Pr^{3+} ions, resulting in enhanced emission intensity. These observations are consistent with the absorption spectra (see Fig. S1 in ESI†).

Fig. 5c and d present 2D temperature-dependent maps of photoluminescence emission (upper panels) and excitation spectra (lower panels) for the $Lu_{1.5}Y_{1.5}Al_{5-x}Sc_xO_{12}$ crystals, where x = 0.0 and 1.5, respectively. The upper panels display emission spectra obtained with an excitation wavelength of 240 nm, while the lower panels show excitation spectra monitored at an emission wavelength of 360 nm. The emission map (upper panel) reveals a dominant broadband emission in the ultraviolet-visible range (300–450 nm), which is assigned to the interconfigurational $4f^15d_1^1 \rightarrow 4f^2$ transitions of Pr^{3+} ions. The intensity of this band is highest at low temperatures and decreases substantially as the temperature increases, reflecting thermal quenching of the interconfigurational $4f^15d_1^1 \rightarrow 4f^2$ emission. Simultaneously, the emission map shows a weaker but noticeable increase in intensity in the visible region (above 450 nm) with increasing temperature, indicating an enhancement of intraconfigurational $4f^2 \rightarrow 4f^2$ transitions within the Pr^{3+} ions. These intraconfigurational $4f^2 \rightarrow 4f^2$ transitions are significantly less efficient than the interconfigurational $4f^15d_1^1 \rightarrow 4f^2$ transition due to parity selection rules. However, with increasing temperature, a thermal population of lower-lying 4f emitting energy states occurs, resulting in increased emission in the visible region. The weaker intensity of the intraconfigurational $4f^2 \rightarrow 4f^2$ transitions compared to interconfigurational $4f^15d_1^1 \rightarrow 4f^2$ transitions at low temperatures results from a lower initial population of these lower-lying 4f energy states.

The excitation maps (lower panels), monitored at emission at 360 nm also show a temperature dependence. The intensity of the excitation bands centered around 240 and 280 nm as well as around 200 nm in Sc admixed crystals, decreases as the temperature increases. This confirms the thermal quenching of the $5d_1$ exited state, consistent with the emission data. The temperature at which the redistribution of emission intensities occurs is strongly influenced by the concentration of Sc^{3+} ions in the crystals. In the Pr^{3+}-doped $Lu_{1.5}Y_{1.5}Al_{5-x}Sc_xO_{12}$ crystal, where x = 0.0, the crossover point of the decrease in the interconfigurational $4f^15d_1^1 \rightarrow 4f^2$ emission and the corresponding increase in intraconfigurational $4f^2 \rightarrow 4f^2$ emission occurs at approximately 170 K. Conversely, in the Pr^{3+}-doped $Lu_{1.5}Y_{1.5}Al_3Sc_{2.0}O_{12}$ (x = 2.0) crystals, this crossover point is observed at around 130 K. For further details, please refer to Fig. S2a–f in ESI.† A maximum PL intensity is observed for the Pr^{3+}-doped $Lu_{1.5}Y_{1.5}Al_4Sc_{1.0}O_{12}$ (x = 1.0) crystal for both emission regions, indicating an optimal level of Sc admixing that enhances radiative transitions while minimizing detrimental non-radiative decay processes. The high spatial resolution photoluminescence spectra of Pr^{3+} ions, recorded in the 460–740 nm spectral range, combined with the estimated radial concentration of Pr^{3+} ions and the degree of host lattice disorder, provide a comprehensive understanding of the influence of Sc^{3+} ions concentration on host lattice disorder and Pr^{3+} ion segregation, refers to Fig. S3a–d and Table S2 in ESI.† This integrated analysis reveals the important role of Sc^{3+} ions admixing in tuning both structural and compositional properties. These findings provide insights into the mechanisms governing the enhancement of emission intensity in luminescent ions, elucidating the relationship between structural modifications and optical properties in doped crystalline systems.

Fig. 5e shows representative decay curves of Pr^{3+} emission at 320 nm, following excitation at 280 nm, for the Pr^{3+}-doped $Lu_{1.5}Y_{1.5}Al_{5-x}Sc_xO_{12}$ crystals, where x = 0.0, 1.0 and 2.0. The emission recorded at 320 nm corresponds to the interconfigurational $4f^15d_1^1 \rightarrow 4f^2$ transition, which occurs on a nanosecond timescale. The decay curves exhibit multi-exponential behavior due to the complex relaxation dynamics of the Pr^{3+} ions in the host crystal. Each curve was fitted using a multi-exponential decay model according to eqn (1). To enable quantitative comparisons of the temperature-dependent evolution of the decay behavior, the effective decay time ($\tau_{effective}$) was computed according to eqn (2). The photoluminescence decay kinetics reveals the trend of decreasing $\tau_{effective}$ with increasing Sc^{3+} ions concentration. At room temperature, $\tau_{effective}$ decreases systematically from 18 ns to 12 nm, for the Pr^{3+}-doped $Lu_{1.5}Y_{1.5}Al_5O_{12}$ (x = 0.0) and $Lu_{1.5}Y_{1.5}Al_3Sc_{2.0}O_{12}$ (x = 2.0) crystals, respectively (see also Fig. S4 in ESI†). Fig. 5f illustrates the temperature dependence of the effective photoluminescence decay time of Pr^{3+} ions emission in the $Lu_{1.5}Y_{1.5}Al_{5-x}Sc_xO_{12}$ crystals, where x ranges from 0.0 to 2.0. The initial effective decay time at low temperatures remains constant at ~18 ns for all examined crystals, corresponding to the radiative decay of the interconfigurational $4f^15d_1^1 \rightarrow 4f^2$ transition. However, with increasing temperature, $\tau_{effective}$ declines, indicating increasing non-radiative relaxation processes. Importantly, the onset of accelerated decay shifts systematically toward lower temperatures as the concentration of Sc^{3+} ions increases. The acceleration of decay time and the reduction in photoluminescence emission intensity with increasing temperature suggest the presence of thermally activated processes. The detailed mechanism responsible for the thermally induced decrease in intensity of the interconfigurational $4f^15d_1^1 \rightarrow 4f^2$ transition, along with the acceleration of decay time values, followed by a systematic increase in emission intensity is observed, originating from the intraconfigurational $4f^2 \rightarrow 4f^2$ transitions and its correlation with the concentration of Sc^{3+} ions. This phenomenon is explained further in the text.

3.3. UV-VIS-NIR emission dynamics of Pr^{3+} ions under synchrotron radiation excitation

The synchrotron radiation excitation spectra, measured at 295 K for Pr^{3+}-doped $Lu_{1.5}Y_{1.5}Al_{5-x}Sc_xO_{12}$ crystals and monitored at emission wavelengths of 314 nm and 610 nm, are presented in Fig. 6a and b, respectively. The excitation spectra monitored at 314 nm emission, displayed in Fig. 6a are consistent with photoluminescence excitation spectra shown in Fig. 5a, c and d. For the Pr^{3+}-doped $Lu_{1.5}Y_{1.5}Al_{5-x}Sc_xO_{12}$ crystal (where x = 0.0), the excitation bands are observed at 4.26 eV and 5.1 eV, which corresponds to the interconfigurational $4f^2 \rightarrow 5d_1^1$

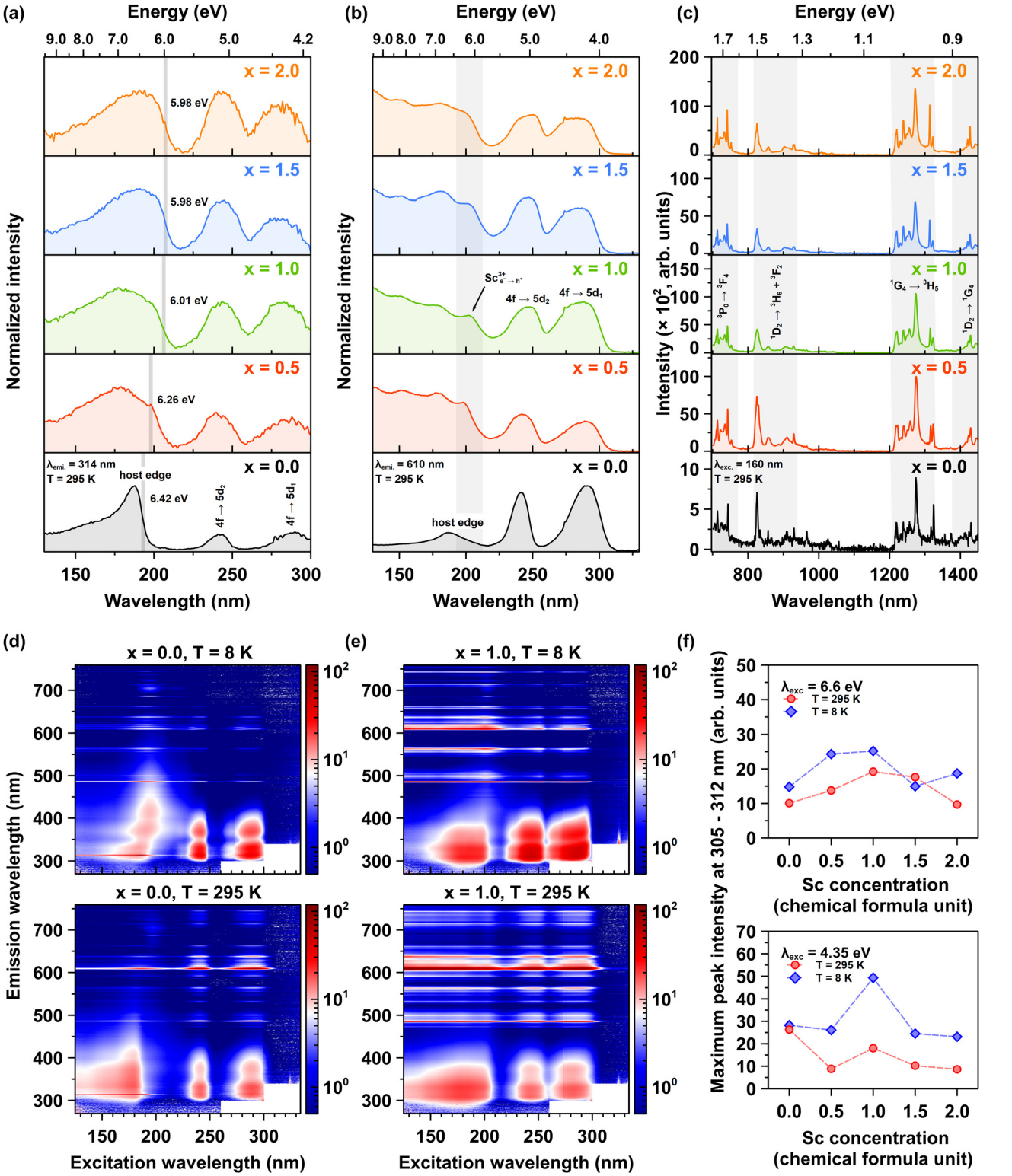

Fig. 6 VUV excitation spectra at 295 K for Pr^{3+}-doped $Lu_{1.5}Y_{1.5}Al_{5-x}Sc_xO_{12}$ crystals, where x = 0.0, 0.5, 1.0, 1.5, 2.0, recorded for emission at (a) 314 nm and (b) 610 nm. (c) NIR luminescence of Pr^{3+} ions excited at 160 nm. 2D excitation–emission maps (EEM) for temperatures of 8 K (upper panels) and 295 K (lower panels) for (d) the Pr^{3+}-doped $Lu_{1.5}Y_{1.5}Al_5O_{12}$ (x = 0.0) and (e) $Lu_{1.5}Y_{1.5}Al_{4.5}Sc_{0.5}O_{12}$ (x = 2.0) crystals, (f) the maximum emission peak intensity in the 305–312 nm spectral range at temperatures of 8 K and 295 K, resulting from interband excitation at 6.6 eV (upper panel) and the interconfigurational $4f^2 \rightarrow 5d_1^1 4f^1$ excitation at energy of 4.35 eV.

$4f^1$ and $4f^2 \rightarrow 5d_2^1 4f^1$ transitions, respectively. The comparatively distinct shape of the bands indicates a relatively ordered crystal lattice environment and a well-defined energy splitting of the 5d energy levels by the crystal field. As the concentration of Sc^{3+} ions progressively increases, the excitation bands exhibit systematic broadening and intensification, indicating a significant enhancement in excitation efficiency. This phenomenon can be attributed to the improved structural coupling between the host lattice and Pr^{3+} ions, which facilitates more efficient energy transfer mechanisms within the crystalline lattice. These observations suggest progressive lattice distortions introduced by Sc^{3+} ions due to their larger ionic radius compared to Al^{3+} ions, Sc^{3+} induces strain in the host lattice and alters the local crystal field symmetry surrounding the Pr^{3+} ions. As a direct consequence, the crystallographic framework exhibits pronounced structural disorder, characterized by significant lattice perturbations. This structural irregularity generates an asymmetric crystal field distribution, ultimately leading to the non-uniform splitting of the $5d^1$ electronic manifold. The excitation spectra monitored at an emission wavelength of 610 nm, as shown in Fig. 6b, reveal similar characteristics to those observed at 314 nm emission. It is important to emphasize that the excitation spectra for Pr^{3+} emission further confirm the presence of a band associated with excitons bound to Sc^{3+} ions. This observation provides additional evidence for the energy transfer mechanism from Sc^{3+}-bound excitons to Pr^{3+} ions, highlighting the role of these excitonic interactions in facilitating the observed emission dynamics.

The host lattice excitation above the 6 eV, corresponding to energy absorption by the host lattice, provides additional insights into the influence of Sc^{3+} ions concentration. For the Pr^{3+}-doped $Lu_{1.5}Y_{1.5}Al_{5-x}Sc_xO_{12}$ crystal (where x = 0.0), the absorption edge is sharp and well-defined, indicating the presence of a structurally ordered lattice. As the Sc^{3+} ions concentration increases, the host absorption edge broadens and shifts slightly to lower energy (see Fig. 6a and b). This effect is pronounced in the excitation spectra for Pr^{3+} ions emission at 610 nm. In the Pr^{3+}-doped $Lu_{1.5}Y_{1.5}Al_{5-x}Sc_xO_{12}$ crystal (where x = 0.0), the host lattice absorption edge exhibits very low intensity, whereas in Sc-admixed crystals, it is significantly enhanced. Additionally, the excitonic band associated with Sc^{3+} ions becomes increasingly pronounced. These features suggest that the intraconfigurational $4f^2 \rightarrow 4f^2$ transitions of Pr^{3+} ions are intensified by the presence of Sc^{3+} ions. This further confirms that Sc^{3+} ions lower the local symmetry and facilitate the transfer of excitation energy toward Pr^{3+} ions, thereby enhancing the same time UV, VIS and NIR emissions (see Fig. 6c). Fig. 6d and e present a comparative analysis of the synchrotron radiation excitation–emission maps recorded at 8 K (upper panels) and 295 K (lower panels) for the Pr^{3+}-doped $Lu_{1.5}Y_{1.5}Al_{5-x}Sc_xO_{12}$ crystals, where x = 0.0 and 1.0. The EEMs reveal that both interconfigurational $4f^1 5d_1^1 \rightarrow 4f^2$ and intraconfigurational $4f^2 \rightarrow 4f^2$ emissions are efficiently excited under intraband excitations (with energies exceeding 188 nm) as well as interconfigurational excitations ($4f^2 \rightarrow 5d_1^1 4f^1$) with energies below 220 nm. Consistent with the observations presented in the photoluminescence emission spectra (refer to Fig. 5b–d), it is evident that the interconfigurational emission bands associated with the transition from $5d_1^1 4f^1$ to $4f^2$ exhibit broadening and a decrease in intensity. Conversely, the intensity of the intraconfigurational $4f^2 \rightarrow 4f^2$ emission increases with the incorporation of Sc^{3+} ions (see also Fig. S5a–c, ESI†). A key observation is the presence of antisite defects (Lu_{Al}^x, Y_{Al}^x) and F^+ center emissions in the 310–450 nm spectral range, which are pronounced at 8 K due to their excitonic character in the Pr^{3+}-doped $Lu_{1.5}Y_{1.5}Al_{5-x}Sc_xO_{12}$ crystal, where x = 0.0.[23,36,58] Conversely, such luminescence is absent in the crystals containing Sc^{3+} ions. Another notable observation is that the Pr^{3+} emission is efficiently excited between 190 and 208 nm, but this phenomenon is exclusive to the Sc-admixed crystals. These findings suggest that Sc^{3+} ions may compete for electronic charge carriers (electrons and holes) with the antisite defects (Lu_{Al}^x, Y_{Al}^x) and F^+ centers, subsequently channeling the excitation energy towards Pr^{3+} ions, thereby enhancing their emission efficiency.

Fig. 6f illustrates the dependence of the maximum peak intensity of Pr^{3+} emission from 305 to 312 nm on the excitation energy, temperature, and Sc^{3+} ions concentration in the crystal lattice. In the case of E_{exc} = 6.6 eV (upper panel), the emission intensity increases systematically with Sc^{3+} ions concentration at both 8 K and 295 K, reaching a maximum value for the Pr^{3+}-doped $Lu_{1.5}Y_{1.5}Al_4Sc_{1.0}O_{12}$ (x = 1.0) crystal. However, across all examined crystals, the emission intensity at 295 K remains considerably lower than at 8 K. Interestingly, for the Pr^{3+}-doped $Lu_{1.5}Y_{1.5}Al_{4.5}Sc_{0.5}O_{12}$ (x = 2.0) crystal, a deviation from the expected trend is observed, as the emission intensity shows an increase at 8 K. This enhanced intensity is likely linked to the formation of a hypoeutectic structure within the crystal lattice, where the incorporation of a perovskite phase and associated excitonic emissions bounded to Sc^{3+} ions in the perovskite phase facilitate energy transfer toward Pr^{3+} ions in the garnet phase.[14] This synergistic energy transfer mechanism amplifies the overall Pr^{3+} emission intensity at 8 K. However, at 295 K, such an enhancement is not observed, as the hypoeutectic structure and the significantly increased lattice disorder notably intensify the intraconfigurational $4f^2 \rightarrow 4f^2$ emission. This suggests that the structural and thermal effects at this temperature play a dominant role in distributing the emission intensities between inter- and intracofigurational transitions of Pr^{3+} ions. For the excitation energy equal to 4.35 eV (lower panel), a different trend emerges regarding the dependence of luminescence intensity on Sc concentration and temperature. At both 8 K and 295 K, the maximum peak intensity decreases with increasing Sc^{3+} ions concentration, except for a notable deviation observed for the Pr^{3+}-doped $Lu_{1.5}Y_{1.5}Al_{5-x}Sc_xO_{12}$ crystal, where x = 1.0. For this crystal, the maximum intensity is observed at 8 K, while at 295 K, the intensity increases but does not reach the highest value. This suggests that specific structural and electronic conditions of Pr^{3+} ions in the $Lu_{1.5}Y_{1.5}Al_4Sc_1O_{12}$ crystal favor efficient radiative emission. However, as the temperature increases to 295 K, luminescence intensity is substantially reduced. The variation in intensity

between the two excitation energies provides further insight into the excitation mechanisms. The significant enhancement of Pr^{3+} emission intensity under excitation at 6.6 eV suggests the presence of an efficient Sc^{3+}-to-Pr^{3+} energy transfer process. This mechanism has not been observed under direct intraconfigurational excitation at 4.35 eV.

The reduction of interconfigurational ($4f^15d_1^1 \rightarrow 4f^2$) emission intensity alongside the increase in intraconfigurational ($4f^2 \rightarrow 4f^2$) emission intensity with rising Sc^{3+} ions concentration and temperature in Pr^{3+}-doped $Lu_{1.5}Y_{1.5}Al_{5-x}Sc_xO_{12}$ crystals is primarily due to enhanced non-radiative relaxation processes facilitated by structural disorder and thermal activation (Fig. 5 and 6). Incorporating Sc^{3+} ions into the crystal lattice substitutes Al^{3+} ions, causing localized lattice distortions because of differences in ionic radii and bonding characteristics. This substitution increases disorder within the crystal lattice, reduces the local symmetry of luminescent centers, and enhances electron–phonon coupling. The altered electronic environment redistributes the electronic density of the excited $5d_1$ state of Pr^{3+} ions. As the temperature rises, thermal energy becomes sufficient to overcome the energy barrier between the excited $5d_1$ state and lower-lying 4f energy states. The enhanced electron–phonon coupling due to Sc-induced disorder facilitates non-radiative relaxation pathways, notably the phonon-mediated crossover decay from the $5d_1^1$ state to the ^3P_J states.[14,59,60] This process leads to a depopulation of the $5d_1^1$ state, resulting in a decreased intensity of the interconfigurational $4f^15d_1^1 \rightarrow 4f^2$ emissions in the ultraviolet region. Simultaneously, these non-radiative processes populate the lower-energy $4f^2$ states. The subsequent radiative relaxation within the $4f^2$ manifold leads to increased emission intensity in the VIS and NIR regions. The presence of Sc^{3+} ions amplifies this effect by promoting stronger electronic coupling between the $5d_1^1$ and $4f^2$ states and increasing the phonon density, which further enhances the likelihood of non-radiative transitions. The acceleration of photoluminescence decay times (see Fig. 5e, f and Fig. S4, ESI†) is directly associated with the increased non-radiative relaxation mechanisms. The intensified electron–phonon interactions and higher thermal energy expedite the de-excitation of the excited states, resulting in shorter decay times. The distinct Pr^{3+} emission dynamics emphasize the key role of Sc admixing in tuning the luminescence properties of Pr^{3+}-doped garnet crystals.

3.4. Temperature dependence of radioluminescence, scintillation and thermoluminescence

Fig. 7a illustrates the room-temperature X-ray-excited luminescence as a function of increasing Sc^{3+} ions concentration. The results are consistent with the photoluminescence (PL) spectra under interconfigurational excitation (Fig. 5a) and interband excitation (Fig. 6a). Notably, the increase in the concentration of Sc^{3+} ions leads to a redistribution of emission intensities between the ultraviolet (UV) and visible (VIS) regions, see also the temperature dependence of 2D RL maps in Fig. S6a–e (ESI†). The underlying mechanism for this redistribution is discussed in detail in Section 3.3. Fig. 7b and c depict the temperature dependence of integrated X-ray-excited luminescence intensities for interconfigurational and intraconfigurational emissions recorded in the 250–450 nm and 470–750 nm spectral regions, respectively. For all Pr^{3+}-doped $Lu_{1.5}Y_{1.5}Al_{5-x}Sc_xO_{12}$ crystals, a similar trend is observed: with increasing temperature, the integrated emission intensity for both inter- and intraconfigurational emissions increases up to approximately 260–280 K, depending on the Sc^{3+} ions concentration. However, the Pr^{3+}-doped $Lu_{1.5}Y_{1.5}A_{5-x}Sc_xO_{12}$ crystal, where $x = 0.0$ exhibits a distinct behavior.

In this case, an increase in integrated emission intensity is observed exclusively for interconfigurational transitions, while the intraconfigurational transitions remain stable across the 10–350 K temperature range. This observation provides additional evidence that Sc-induced lattice disorder facilitates an increased population of lower-energy 4f states, a process mediated by phonon interactions. The temperature-dependent variation in emission intensity is closely linked to the energy depth of charge trapping centers. At elevated temperatures, shallow traps, such as those associated with Lu_{Al}^x and Y_{Al}^x dislocations, become inactive in capturing electrons because the thermal energy exceeds the energy barriers of these traps. Consequently, the excitation energy is efficiently transferred to Pr^{3+} ions, resulting in a maximized emission intensity. This interplay underscores the role of temperature in modifying the efficiency of energy transfer and emission efficiency. This mechanism is corroborated by the TL glow curves obtained after X-ray excitation at 10 K, as shown in Fig. 7d. The primary TL band is observed between 80 and 300 K, corresponding to the temperature range where the radioluminescence intensity increases. Another significant observation is that Sc admixing does not substantially modify the trap depth distribution and density in the temperature range of 10–300 K. The observed TL glow curves can be attributed to the formation of shallow electron trapping centers in Lu_{Al}^x and Y_{Al}^x dislocations.[58,61] Similarly, in the high-temperature region (300–700 K), as illustrated in Fig. 7e, the distribution and density of deep trapping centers remains largely unaffected by Sc admixing. These deep trapping centers, responsible for the high-temperature TL glow curves, originate from oxygen vacancies ($V_O^{\bullet\bullet}$) and transition ion impurities.[62,63] The incorporation of Sc^{3+} ions demonstrates minimal impact on the formation of shallow trapping centers, evidenced by the relatively constant trap density across all crystals, as shown in Fig. 7f (upper panel). In contrast, Sc admixing significantly reduces the density of deep trapping centers within the crystal structure, as depicted in Fig. 7f (lower panel). Quantitatively, the integrated TL intensity in Sc-admixed crystals exhibits approximately an order of magnitude reduction compared to Pr^{3+}-doped $Lu_{1.5}Y_{1.5}A_{5-x}Sc_xO_{12}$ crystal (where $x = 0.0$), as demonstrated in Fig. 7f (lower panel).

Thermoluminescence is a valuable technique for elucidating the role of charge carriers in the scintillation process. Shallow traps are typically associated with the slow components observed in scintillation decay curves,[64] while deep traps, identified through high-temperature thermoluminescence measurements exceeding 300 K, are correlated with a decrease in scintillation

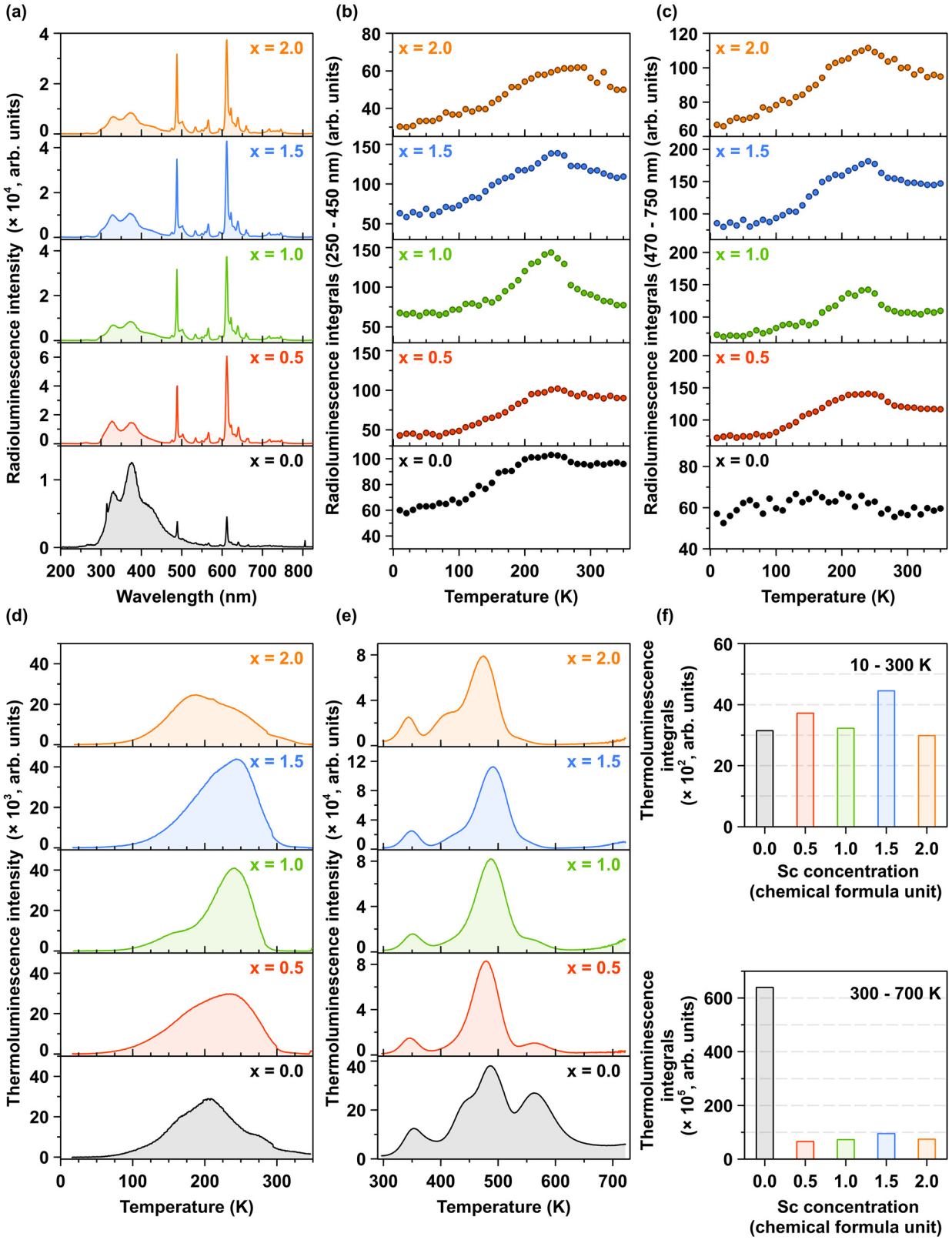

Fig. 7 (a) Room temperature RL spectra of Pr^{3+}-doped $Lu_{1.5}Y_{1.5}Al_{5-x}Sc_xO_{12}$ crystals, where x = 0.0, 0.5, 1.0, 1.5, 2.0, (b) temperature-dependent integrated emission intensities of the interconfigurational $4f^15d_1^1 \rightarrow 4f^2$ transitions in the 250–450 nm spectral range, (c) temperature-dependent integrated intensities of the intraconfigurational $4f^2 \rightarrow 4f^2$ transitions within the range of 470–750 nm. (d) Low-temperature (10–310 K) TL curves following irradiation at 10 K. (e) High-temperature (310–700 K) TL curves following irradiation at 310 K. (f) Integrated TL intensities between 10–300 K (upper panel) and 300–700 K (lower panel) for Pr^{3+}-doped $Lu_{1.5}Y_{1.5}Al_{5-x}Sc_xO_{12}$ crystals with increasing Sc^{3+} ions concentration.

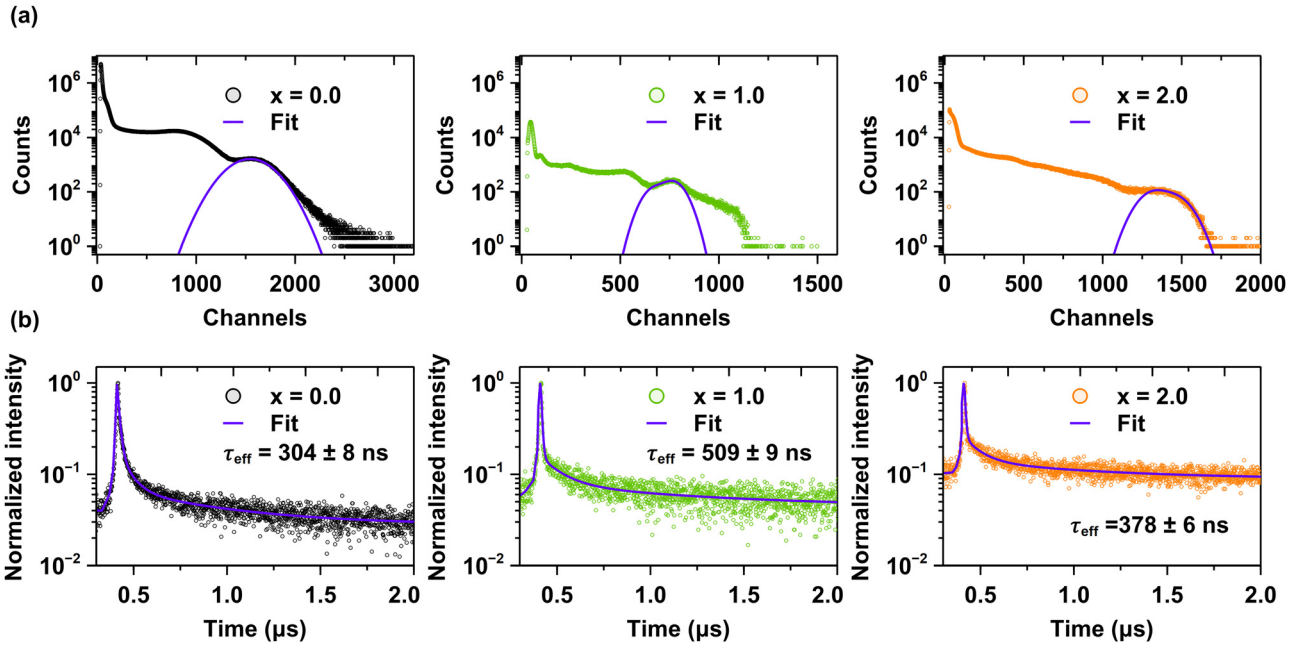

Fig. 8 (a) Scintillation light yield values, and (b) decay kinetics under excitation with γ-rays from the ^{137}Cs radionuclide (662 keV) for the Pr^{3+}-doped $Lu_{1.5}Y_{1.5}Al_{5-x}Sc_xO_{12}$ crystals, where x = 0.0, 1.0 and 2.0.

light yield.[62] The experimental data demonstrate a significant correlation between the reduced density of deep trapping centers and enhanced scintillation parameters in Sc-admixed crystals, as evidenced in Fig. 8a, b and Fig. S7a (ESI†)-as well as Table 1.

Fig. 8a and Fig. S7a in ESI† present the pulse height spectra measured using a ^{137}Cs radioisotope with an amplifier shaping time of 2 μs. Fig. 8b and Fig. S7b (ESI†) compare the scintillation decay times of crystals with increasing Sc concentrations. The key scintillation parameters, including light yield, decay times, and energy resolution, are summarized in Table 1 as a function of Sc^{3+} ions concentration. As discussed in previous sections, the scintillation properties are also significantly influenced by Sc admixing. Specifically, the light yield value increases approximately sixfold in the Pr^{3+}-doped $Lu_{1.5}Y_{1.5}Al_{5-x}Sc_xO_{12}$ crystals for the x ranging from 0.5 to 1.5, reaching a maximum value for the Pr^{3+}-doped $Lu_{1.5}Y_{1.5}Al_{3.5}Sc_{1.5}O_{12}$ crystal (x = 1.5). Although the Pr^{3+}-doped $Lu_{1.5}Y_{1.5}Al_3Sc_2O_{12}$ hypoeutectic crystal (x = 2.0) also exhibits an enhanced light yield, the improvement is less pronounced compared to single-phase crystals. The substantial increase in light yield for Sc-admixed crystals is attributed to the $\left(Sc_{e^-\rightarrow h^+}{}^{3+} \rightarrow Pr^{3+}\right)$ energy transfer process (Fig. 5 and 6) and reduced density of deep trapping centers, as evidenced by high-temperature TL glow curves (Fig. 7e). Additionally, the effective scintillation decay times are approximately doubled following Sc admixing, indicating significant modifications to the energy transfer dynamics. These strong dependencies of scintillation properties on Sc concentration lead to two key conclusions: (i) the local distortions introduced by Sc^{3+} ions effectively compete with other trapping centers, such as dislocations, oxygen vacancies, and trace impurities, in capturing charge carriers. (ii) Excitons bound to Sc^{3+} ions efficiently transfer their energy to Pr^{3+} ions, thereby enhancing scintillation efficiency.[30] Furthermore, Sc admixing significantly improves the energy resolution of the crystals, further demonstrating the beneficial impact of Sc incorporation on scintillation performance.

3.5. Electron paramagnetic resonance

Electron paramagnetic resonance spectra were recorded for all examined crystals. The EPR spectrum of the Pr^{3+}-doped $Lu_{1.5}Y_{1.5}A_{5-x}Sc_xO_{12}$, where x = 0.0 exhibits a complex multiplet structure, as illustrated in Fig. 1, comprising numerous

Table 1 Scintillation decay times, light yield values (shaping time 2 μs), energy resolution (%) and standard error values (err.) for the Pr^{3+}-doped $Lu_{1.5}Y_{1.5}Al_{5-x}Sc_xO_{12}$ crystals with increasing Sc^{3+} ions concentration under γ-ray excitation from ^{137}Cs radioisotope

Sc concentration (chemical formula unit)	Scintillation parameters					
	τ_1/err. (ns)	τ_2/err. (ns)	τ_3/err. (ns)	τ_{eff}/err. (ns)	LY/err. (phs/eV, 2 μs)	Energy res. (%)
0.0	10 ± 1.2	62 ± 5.4	459 ± 16	304 ± 8	1800 ± 90	27
0.5	16 ± 2.4	87 ± 1.8	613 ± 11	534 ± 5	9700 ± 480	18
1.0	9 ± 0.8	106 ± 8.7	629 ± 17	509 ± 9	9500 ± 470	14
1.5	7 ± 1.1	64 ± 2.6	572 ± 14	516 ± 7	11 200 ± 560	15
2.0	5 ± 0.6	58 ± 3.1	467 ± 10	378 ± 6	6700 ± 330	14

overlapping resonance signals. These spectral features are tentatively ascribed to paramagnetic centers associated with Mn^{2+} ions.

To validate this observation, the experimental spectrum was approximated using a calculated spectrum based on the following spin-Hamiltonian:

$$\hat{H} = g\beta\hat{S}_z B + A\hat{S}_z\hat{I}_z + B_4^0 + O_4^0 \quad (5)$$

where g, β, $\hat{S}_z$, $\hat{I}_z$, B, A, B_4^0, O_4^0 are g factor, Bohr magneton, z component of the electron and nuclear spin operators, resonance magnetic field, hyperfine constant (in the present case it is for ^{55}Mn nucleus with the nuclear spin $I = 5/2$ and natural abundance of 100%), cubic zero-field splitting constant (cubic constant are provided further in the text) and Stevens operator, respectively. Three distinct converged simulations were required (corresponding to three different Mn^{2+} centers, denoted as $Mn_{1-3}{}^{2+}$ in Fig. 9a to accurately approximate the experimental spectrum shown in Fig. 9a. The summation of the three calculated spectra demonstrates good agreement with the experimental data. However, notable intensity discrepancies are observed in the extreme low and high magnetic field regions (below 2000 G and above 6000 G), where the experimental spectrum exhibits significantly higher intensity (as evidenced in the magnified spectrum in Fig. 9a. These result from the limitations of calculations resulting in the increased transition probability compared to experimental observations. Furthermore, the broadening of resonance lines at higher magnetic fields leads to decreased peak-to-peak intensity.[65,66] The parameters used for the calculations are summarized in Table 2.

The observed hyperfine constant exhibits values characteristic of Mn^{2+}. The cubic constant demonstrates notable variation among centers: it is relatively small for $Mn_1{}^{2+}$ but approximately two orders of magnitude larger for $Mn_{2,3}{}^{2+}$. Such large cubic constants, reaching hundreds of MHz, have been previously reported.[67] Furthermore, the cubic constant displays opposite signs for $Mn_{2,3}{}^{2+}$ as compared to the $Mn_1{}^{2+}$. Notably, neither axial ($B_2{}^0$) nor ($B_2{}^2$) rhombic constants were required to accurately describe the experimental spectrum for any of the three $Mn_{1-3}{}^{2+}$ centers. These observations collectively suggest that all three centers occupy highly symmetric sites within the LuAG lattice. The centers can only occupy octahedral and tetrahedral alumina positions. The Al–O bond length is larger in the case of octahedral position as compared to the tetrahedrala sites as reported in the isostructural YAG.[68] Given that the cubic constant is inversely proportional to the fifth power of the bond length, in can be assumed that the $Mn_1{}^{2+}$ center occupies the octahedral site, while $Mn_{2,3}{}^{2+}$ are situated at tetrahedral sites. The notably larger cubic constant observed for $Mn_3{}^{2+}$ compared to $Mn_2{}^{2+}$ suggests a reduction in the Mn–O bond

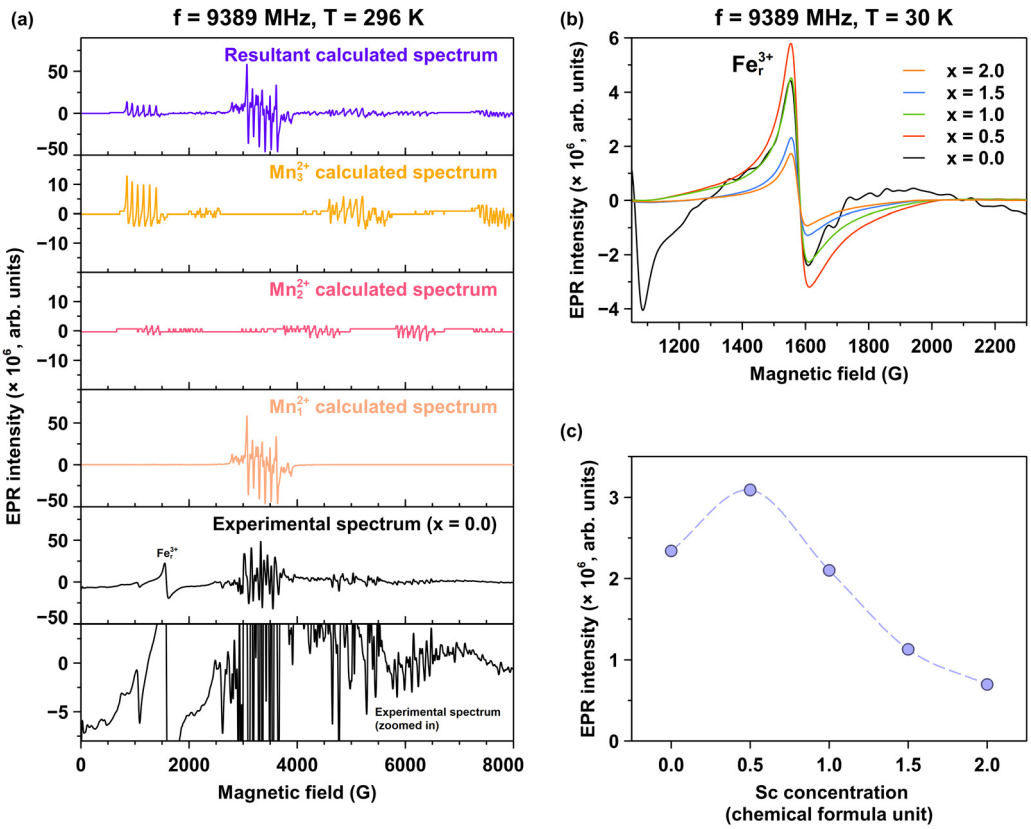

Fig. 9 (a) Experimental (Exp.) and calculated (Calc1–3 and Calc_All; Calc_All is the sum of the Calc1–3) EPR spectra of the Pr^{3+}-doped $Lu_{1.5}Y_{1.5}A_5O_{12}$ (x = 0.0). The experimental spectrum is magnified to highlight the details of the weakest spectral components. Three distinct but partially overlapping Mn^{2+} spectral contributions ($Mn_{1-3}{}^{2+}$) are presented. The label $Fe_r{}^{3+}$ corresponds to the signal originating from rhombic Fe^{3+} sites.[65] (b) $Fe_r{}^{3+}$ signal in the Pr^{3+}-doped $Lu_{1.5}Y_{1.5}A_{5-x}Sc_xO_{12}$ crystals with increasing Sc^{3+} ions concentration, (c) dependence of the double integral intensity of the $Fe_r{}^{3+}$ signal on the Sc concentration.

length, which may be attributed to the presence of a highly symmetric perturbation in the vicinity of the Mn_3^{2+} position within the lattice structure. The incorporation of Sc results in the complete disappearance of the Mn^{2+} spectrum. This phenomenon can be attributed to Sc substitution at octahedral Al sites, thereby preventing the incorporation of Mn^{2+} ions (which is considered a trace impurity) into this crystallographic position.

A signal corresponding to a g factor of 4.3 ($\sim$1600 G), identified as Fe_r^{3+} in Fig. 9b, is attributed to rhombic Fe^{3+}.[65] Notably, this signal is also detected in the Sc admixed samples. To facilitate a more detailed investigation, the Fe_r^{3+} signals for all samples are depicted in Fig. 9c. The origin of the rhombic Fe_r^{3+} signal is likely associated with the crystal surface, where structural disorder is pronounced, even though EPR inherently measures bulk properties. It is evident that the degree of Sc^{3+} ions concentration significantly influences the Fe_r^{3+} signal. To illustrate this effect, Fig. 9c shows the dependence of the double integral intensity of the Fe_r^{3+} signal (which is directly proportional to the concentration of paramagnetic centers[69]) on the Sc atoms concentration. Specifically, a Sc^{3+} ions concentration equal to 0.5 leads to an approximately 1.5-fold increase in the Fe_r^{3+} signal intensity. Beyond this point, the signal intensity decreases with further increases in Sc^{3+} ions concentration. This trend suggests that Sc admixing may inhibit the incorporation of trace impurities (*e.g.* Fe^{3+} and Mn^{2+}), particularly at the crystal rim, thereby reducing the concentration of Fe_r^{3+} paramagnetic centers. Consequently, this leads to an improvement in the scintillation performance. This interpretation is consistent with the scintillation and thermoluminescence characteristics presented in Fig. 7 and 8. Furthermore, the theoretical calculations of the experimentally recorded EPR spectra provide additional validation for the presence of all paramagnetic centers listed in Table 2 and their dependence on Sc concentration (see Fig. S8a–c, in the ESI† and the related discussion). A particularly noteworthy observation is the correlation between the dependence of the double integral intensity on the Sc^{3+} ions concentration for both the O^- defect and the F^+ center (Fig. S8a and b, ESI†). These defect-related contributions exhibit a similar trend and comparable double integral intensity, suggesting a possible charge transfer mechanism: $O^{2-} + h^+ \rightleftharpoons V_0^{2+} + e^-$. Additionally, a strong correlation is observed between the dependence of the double integral intensity on the Sc^{3+} ions concentration for the F^+ and O^- centers and the variation in luminescence intensity of fits 1–4, as shown in Fig. S9a–d in the ESI.† Notably, the behavior of the F^+ and O^- centers closely follows that of luminescence fit 4, providing compelling evidence that fit 4 originates from the F^+–O^- defect pair.

Table 2 Spin-Hamiltonian parameters derived from eqn (5). The error is ±0.02 for the g factor (applicable to all centers), ±10 MHz for the hyperfine constant (for all centers), and ±0.1 MHz for the cubic constant (Mn_1^{2+}) and ±10 MHz for the cubic constants ($Mn_{2,3}^{2+}$)

Paramagnetic centers	g tensor/factor				
	g_1	g_2	g_3	A (MHz)	B_4^0 (MHz)
Mn_1^{2+}	2.00			300	6.0
Mn_2^{2+}	1.99			300	−100
Mn_3^{2+}	1.99			300	−170
F^+	1.999			n/a	n/a
O^-	2.03			n/a	
Lu^{2+}	1.93	1.96	1.99	300	
Ir^{4+}	1.86			n/a	
$O_2^-{}_{OH}$	1.93	1.96	1.99	1700	

4. Conclusions

The crystallization of materials containing strongly mismatched elements occupying identical crystallographic sites presents significant challenges in achieving good structural homogeneity, particularly when using the micro-pulling-down (μ-PD) method. This investigation addressed these challenges by examining the crystallization process from melts containing highly incompatible elements Sc and Al, which occupy the same octahedral sites within the Pr^{3+}-doped $Lu_{1.5}Y_{1.5}Al_{5-x}Sc_xO_{12}$ garnet lattice (where x = 0.0, 0.5, 1.0, 1.5, and 2.0). To address the significant issue of radial elemental inhomogeneity, a critical barrier in the μ-PD crystal growth process, a modified crucible design with five independent crystallization capillaries was used. The implementation of five crystallization capillaries revealed the formation of heterogeneous, round-like spots whose occurrence varied randomly with the increasing Sc^{3+} ions concentration. The random distribution of these heterogeneous spots further indicated non-uniform ejection dynamics, suggesting that the melt within the crucible exhibited localized heterogeneity. This heterogeneity was likely attributable to the ionic radii mismatch between Sc and Al elements, which disrupts the uniformity of the melt composition and influences the crystallization process. This finding highlighted the importance of thoroughly mixing raw materials prior to melting, even in the μ-PD method, where the initial material weight was approximately 1 gram, to achieve improved elemental homogeneity. Another significant observation was the identification of a threshold concentration of Sc^{3+} ions at x = 1.5. The key finding revealed that at Sc^{3+} ion concentrations exceeding this threshold, the ionic mismatch induced thermodynamic processes that preferentially facilitated the formation of a garnet/bixbyite-like distorted perovskite hypoeutectic crystal structure, rather than promoting further substitution of Sc^{3+} for Al^{3+} ions within the lattice. This discovery provides a novel perspective on exploting ionic radii mismatch as an approach for the controlled crystallization of eutectic and hypoeutectic crystals, potentially advancing materials engineering methodologies. Moreover, the independent crystallization observed in each capillary presented a promising opportunity to enhance the self-organization of non-mixing phases during the crystallization of hypoeutectic crystals, offering valuable insights for optimizing crystal growth processes. Vibrational spectroscopy confirmed that the progressive substitution of Sc^{3+} for Al^{3+} ions increased the host lattice disorder, with saturation occurring at Sc^{3+} ions concentrations of $x \geq 1.0$. This enhanced lattice

disorder significantly lowered the local symmetry around Pr^{3+} ions, directly affecting the crystal field strength and tuning the energetic positioning of the $5d_1^1$ excited state of Pr^{3+} ions relative to the conduction band minimum. The incorporation of Sc^{3+} ions reduced local symmetry around Pr^{3+} ions, lowering the energy barrier between the $5d_1^1$ excited state and the lower-lying 4f energy state. This reduction facilitated non-radiative pathways, enabling the $5d_1^1$ to ^3P_J crossover of excited electrons. This significantly enhanced the Pr^{3+} emission intensity within the VIS and NIR spectral ranges, demonstrating its potential for tuning luminescent properties through controlled lattice disorder. For the first time, the $Sc_{e^- \rightarrow h^+}{}^{3+} \rightarrow Pr^{3+}$ energy transfer mechanism was experimentally validated through excitation spectroscopy using synchrotron radiation. This mechanism resulted in a sixfold enhancement of the scintillation light yield, reaching a maximum value of 11 200 photons per MeV in the Pr^{3+}-doped $Lu_{1.5}Y_{1.5}Al_{5-x}Sc_xO_{12}$ crystal where x = 1.5. This enhancement was accompanied by an approximate doubling of the scintillation response time. Synchrotron radiation excitation–emission mapping revealed that local lattice distortions induced by Sc^{3+} ions effectively competed with trapping centers (dislocations, oxygen vacancies, and trace impurities) in charge carrier capture processes. This competitive mechanism enhanced energy transfer efficiency to Pr^{3+} ions, resulting in significantly improved scintillation properties. The findings demonstrated the crucial role of controlled lattice modification in optimizing energy transfer pathways and enhancing luminescent performance. Thermoluminescence glow curve analysis revealed that trapping centers associated with Lu_{Al}^{x} and Y_{Al}^{x} dislocations dominated below 200 K, while oxygen vacancies $\left(V_O^{\bullet\bullet}\right)$ combined with other trapping centers were prominent above 280 K. Sc admixing had a negligible effect on the formation of shallow trapping centers. However, in the case of deep trapping centers, Sc incorporation significantly reduced their density by approximately an order of magnitude compared to the Sc-free crystal. This significant reduction underscores a key role of Sc admixing in mitigating deep trapping centers, thereby optimizing charge carrier dynamics and enhancing scintillation performance. The incorporation of Sc^{3+} into the garnet lattice systematically reduced the concentration of Mn^{2+} and Fe^{3+} trace impurities, which acted as detrimental trapping centers, thereby improving scintillation light yield. EPR spectroscopy further revealed that synergistic interactions between F^+ centers and Pr^{3+} ions amplified the Pr^{3+}-related emission intensity at 370 nm, corroborating historical assignments from late 20th-century studies. Importantly, the emission band at 410–420 nm, previously misattributed to isolated F^+ centers in post-1990s literature, was conclusively linked to F^+–O^- defect pairs. This discovery resolved long-standing ambiguities in defect-related luminescence mechanisms in garnet materials and highlighted the need for precise spectroscopic characterization to avoid erroneous defect assignments. The findings advocated for revised analytical frameworks in the study of garnet scintillators, emphasizing the critical role of defect pair interactions in governing emission properties. The demonstrated resilience of the Sc-admixed system against shallow trapping centers formation, coupled with its ability to suppress the influence of deep trapping centers and facilitate Sc-mediated energy transfer processes, represents a crucial advancement for the design of next-generation oxide scintillators and phosphors materials. Furthermore, the controlled tuning of host lattice disorder through Sc incorporation enables precise adjustments to structural, scintillation, and luminescence properties. This approach not only enhances the luminescence intensity of rare-earth elements but also significantly improves the material suitability for targeted applications, marking a step forward in the development of advanced scintillators and luminescent materials.

Author contributions

Karol Bartosiewicz: conceptualization, methodology, investigation, formal analysis, writing – original draft, writing – review & editing, project administration, supervision, corresponding author. Yevheniia Smortsova: investigation, data curation, formal analysis, writing – review & editing. Piotr Radmoski: investigation, data analysis, writing – review & editing. Marcin E. Witkowski: investigation, data analysis, writing – review & editing. Konrad J. Drozdowski: investigation, data analysis, writing – review & editing. Masao Yoshino: investigation, resources, writing – review & editing. Takahiko Horiai: investigation, validation, writing – review & editing. Damian Szymański: investigation, data analysis, writing – review & editing. Wioletta Dewo: investigation, data analysis, writing – review & editing. Justyna Zeler: investigation, data analysis, writing – review & editing. Paweł Socha: investigation, data analysis, writing – review & editing. Maksym Buryi: investigation, writing – review & editing. Andrey Prokhorov: methodology, writing – review & editing. David John: data analysis, writing – review & editing. Jakub Volf: investigation (Scintillation measurements), writing – review & editing. Tomasz Runka: investigation, data analysis, writing – review & editing. Tomasz Pędziński: investigation, writing – review & editing. Karol Hauza: investigation, writing – review & editing. Vítězslav Jarý: investigation, writing – review & editing. Yasuhiro Shoji: resources, writing – review & editing. Kei Kamada: resources, writing – review & editing. Eugeniusz Zych: writing – review & editing. Winicjusz Drozdowski: writing – review & editing. Akira Yoshikawa: resources, writing – review & editing.

Data availability

Upon acceptance of the manuscript for publication, all raw data supporting the findings of this study will be made available in the ASEP repository, provided by the Institute of Physics of the Czech Academy of Sciences, Prague, Czech Republic. Below is the DOI corresponding to the raw data: DOI: **https://doi.org/10.57680/asep.0635702**, Handle: **https://hdl.handle.net/11104/0366734**. The repository includes a short description of how to access and interpret the data. The files are organized into separate zipped folders, each containing specific data as presented in the manuscript. For further inquiries regarding data access, please contact the corresponding author, Karol Bartosiewicz, *via* email at bartosiewicz@fzu.cz. Alternatively, you can

refer to the ASEP repository guidelines available at **https://asep-portal.lib.cas.cz/** or reach out to the ASEP repository support team *via* email at arl@lib.cas.cz.

Conflicts of interest

The authors declare that they have no known competing financial interests or personal relationships that could have appeared to influence the work reported in this paper.

Acknowledgements

This project has received funding from the European Union's Horizon Europe research and innovation programme under the Marie Skłodowska-Curie Actions COFUND, Physics for Future, grant agreement No. 101081515, the National Science Centre Poland (NCN) No. 2020/39/D/ST3/02711 as well as the GIMRT program of the Institute for Materials Research, Tohoku University Proposal No. 202306-RDKYA-0533. The financial support of the Leading Agency National Science Centre – Czech Science Foundation Project No. 24-14580L is gratefully acknowledged.

References

1 M. Nikl, A. Yoshikawa, K. Kamada, K. Nejezchleb, C. R. Stanek, J. A. Mares and K. Blazek, *Prog. Cryst. Growth Charact. Mater.*, 2013, **59**, 47–72.
2 C. Dujardin, E. Auffray, E. Bourret-Courchesne, P. Dorenbos, P. Lecoq, M. Nikl, A. N. Vasil'ev, A. Yoshikawa and R. Y. Zhu, *IEEE Trans. Nucl. Sci.*, 2018, **65**, 1977–1997.
3 G. Bizarri, *J. Cryst. Growth*, 2010, **312**, 1213–1215.
4 K. Bartosiewicz, H. Takahiko, Y. Akihiro, A. Yoshikawa, S. Kurosawa, M. Yoshino and Y. Zorenko, *Mater. Sci. Eng., B*, 2020, **261**, 114677.
5 K. Bartosiewicz, A. Markovskyi, T. Horiai, D. Szymański, S. Kurosawa, A. Yamaji, A. Yoshikawa and Y. Zorenko, *J. Alloys Compd.*, 2022, **905**, 164154.
6 I. Carrasco, K. Bartosiewicz, M. Nikl, F. Piccinelli and M. Bettinelli, *Opt. Mater.*, 2015, **48**, 252–257.
7 P. Bolek, Z. Justyna, J. Trojan-Piegza, L. D. Carlos and E. Zych, *Chem. Eng. J.*, 2021, **421**, 129764.
8 Y. Kanke and A. Navrotsky, *J. Solid State Chem.*, 1998, **141**, 424–436.
9 K. Bartosiewicz, A. Szysiak, R. Tomala, P. Gołębiewski, H. Węglarz, V. Nagirnyi, M. Kirm, I. Romet, M. Buryi, V. Jary, R. Kucerkova, M. Wzorek and R. Buczyński, *Phys. Rev. Appl.*, 2023, **20**, 014047.
10 Z. Hu, X. Chen, H. H. Chen, Y. Shi, X. Liu, T. Xie, H. Kou, Y. Pan, E. Mihóková, M. Nikl and J. Li, *J. Lumin.*, 2019, **210**, 14–20.
11 W. Drozdowski, K. Brylew, A. J. Wojtowicz, J. Kisielewski, M. Świrkowicz, T. Łukasiewicz, J. T. M. de Haas and P. Dorenbos, *Opt. Mater. Express*, 2014, **4**, 1207.
12 M. V. Derdzyan, K. L. Ovanesyan, A. G. Petrosyan, A. Belsky, C. Dujardin, C. Pedrini, E. Auffray, P. Lecoq, M. Lucchini and K. Pauwels, *J. Cryst. Growth*, 2012, **361**, 212–216.
13 C. Foster, Y. Wu, L. Stand, M. Koschan and C. L. Melcher, *J. Lumin.*, 2019, **216**, 116751.
14 K. Bartosiewicz, B. Albini, D. Szymański, P. Socha, T. Horiai, M. Yoshino, A. Yamaji, S. Kurosawa, R. Kucerkova, P. Galinetto and A. Yoshikawa, *J. Alloys Compd.*, 2024, **985**, 174078.
15 R. D. Shannon, *Acta Crystallogr., Sect. A*, 1976, **32**, 751–767.
16 E. Mihóková, V. Babin, K. Bartosiewicz, L. S. Schulman, Č. Václav, K. Miroslav and M. Nikl, *Opt. Mater.*, 2015, **40**, 127–131.
17 M. Fasoli, A. Vedda, M. Nikl, C. Jiang, B. P. Uberuaga, D. A. Andersson, K. J. McClellan and C. R. Stanek, *Phys. Rev. B:Condens. Matter Mater. Phys.*, 2011, **84**, 081102(R).
18 E. Mihóková, A. Vedda, M. Fasoli, F. Moretti, A.-L. Bulin, M. Nikl, M. Bettinelli, A. Speghini, H. Ogino and A. Yoshikawa, *Opt. Mater.*, 2010, **32**, 1298–1301.
19 H. Ogino, K. Kamada, A. Yoshikawa, F. Saito, J. Pejchal, J. A. Mares, M. Nikl, A. Vedda, J.-I. Shimoyama and K. Kishio, *IEEE Trans. Nucl. Sci.*, 2008, **55**, 1197–1200.
20 K. Kamada, T. Yanagida, J. Pejchal, M. Nikl, T. Endo, T. Kousuke, Y. Fujimoto, F. Akihiro and A. Yoshikawa, *IEEE Nuclear Science Symposium Conference Record*, 2011, DOI: **10.1109/nssmic.2011.6154631**.
21 K. Kamada, T. Yanagida, J. Pejchal, M. Nikl, T. Endo, T. Kousuke, Y. Fujimoto, F. Akihiro and A. Yoshikawa, *IEEE Trans. Nucl. Sci.*, 2012, **59**, 2130–2134.
22 C. Hu, X. Feng, J. Li, A. Vedda, D. Ding, Z. Zhou, H. Kou and Y. Pan, *Phys. Rev. Appl.*, 2016, **6**, 064026.
23 K. Bartosiewicz, T. Horiai, A. Yamaji, A. Yoshikawa, S. Kurosawa, M. Yoshino and Y. Zorenko, *Mater. Sci. Eng., B*, 2020, **261**, 114677.
24 K. Bartosiewicz, K. Bartosiewicz, V. Fritz, V. Fritz, D. V. D. Heggen, D. V. D. Heggen, D. Szymanski, D. Szymanski, J. Zeler, J. Zeler, J. Pejchal, J. Pejchal, A. Yamaji, A. Yamaji, R. Kucerkova, R. Kucerkova, A. Beitlerova, A. Beitlerova, S. Kurosawa, S. Kurosawa, A. Yoshikawa, A. Yoshikawa, P. F. Smet, P. F. Smet, E. Zych, E. Zych, M. Nikl and M. Nikl, *J. Mater. Chem. C*, 2023, **11**, 8850–8865.
25 K. Bartosiewicz, *Metals*, 2023, **13**, 422.
26 V. Laguta, M. Buryi, V. Babin, P. Machek, S. Zazubovich, K. Bartosiewicz, S. Kurosawa, A. Yamaji, A. Yoshikawa, K. Ulicná, V. Chlan, H. Štěpánková and M. Nikl, *J. Mater. Chem. C*, 2023, **11**, 1346–1359.
27 Y. O. Zagorodniy, V. Chlan, H. Stepánková, Y. Fomichov, J. Pejchal, V. V. Laguta and M. Nikl, *J. Phys. Chem. Solids*, 2019, **126**, 93–104.
28 K. Bartosiewicz, V. Fritz, D. Van, D. Szymański, Z. Justyna, Y. Akihiro, J. Pejchal, R. Kučerková, A. Beitlerová, S. Kurosawa, A. Yoshikawa, P. Smet, E. Zych and M. Nikl, *J. Mater. Chem. C*, 2023, **11**, 8850–8865.
29 K. Miroslav, M. Nikl, P. Průša, J. Mareš, K. Nitsch, M. Hanuš, O. Zuzana and R. Kučerková, *J. Cryst. Growth*, 2011, **318**, 813–819.
30 K. Miroslav, P. Průša, J. Mareš, M. Nikl, K. Nitsch, M. Hanuš, O. Zuzana and R. Kučerková, *IOP Conf. Ser.:Mater. Sci. Eng.*, 2010, **15**, 012012.

31 P. Veber, K. Bartosiewicz, J. Debray, G. Alombert-Goget, O. Benamara, V. Motto-Ros, T. Mai Pham, A. Borta-Boyon, H. Cabane, L. Kheirréddine, L. Franck, K. Kamada, A. Yoshikawa and M. Maglione, *CrystEngComm*, 2019, **21**, 3844–3853.
32 A. Markovskyi, W. Gieszczyk, P. Bilski, A. Fedorov, K. Bartosiewicz, K. Paprocki, T. Zorenko and Y. Zorenko, *J. Alloys Compd.*, 2020, **849**, 155808.
33 K. Bartosiewicz, V. Babin, A. Beitlerova, P. Bohacek, K. Jurek and M. Nikl, *J. Lumin.*, 2017, **189**, 126–139.
34 J. Sanders, Veusz, **https://veusz.github.io/**, (accessed June 4, 2025).
35 M. N. Magomedov, *Solid State Commun.*, 2020, **322**, 114060.
36 K. Bartosiewicz, T. Horiai, A. Yamaji, A. Yoshikawa, S. Kurosawa, K. J. Kim, V. Vistovskyy, A. Voloshinovskii and Y. Zorenko, *J. Lumin.*, 2021, 235.
37 K. Bartosiewicz, V. Babin, K. Kamada, A. Yoshikawa, A. Beitlerova and M. Nikl, *Opt. Mater.*, 2018, **80**, 98–105.
38 K. Bartosiewicz, V. Babin, K. Kamada, A. Yoshikawa, J. A. Mares, A. Beitlerova and M. Nikl, *Opt. Mater.*, 2017, **63**, 134–142.
39 K. Bartosiewicz, A. Markovskyi, T. Zorenko, A. Yoshikawa, S. Kurosawa, A. Yamaji and Y. Zorenko, *Phys. Status Solidi RRL*, 2020, **14**, 2000327.
40 K. Bartosiewicz and K. Bartosiewicz, *Metals*, 2023, **13**, 422.
41 D. L. Rousseau, R. P. Bauman and S. P. S. Porto, *J. Raman Spectrosc.*, 2005, **10**, 253–290.
42 K. Papagelis, G. Kanellis, S. Ves and G. A. Kourouklis, *Phys. Status Solidi B*, 2002, **233**, 134–150.
43 W. Dewo, K. Luczynska, Y. Zorenko, V. Gorbenko, K. Druzbicki and T. Runka, *Spectrochim. Acta, Part A*, 2020, **231**, 118111.
44 A. Markovskyi, P. Radomski, W. Dewo, V. Gorbenko, A. Fedorov, T. Runka and Y. Zorenko, *Mater. Res. Bull.*, 2025, **182**, 113141.
45 M. Poulos, S. Giaremis, J. Kioseoglou, J. Arvanitidis, D. Christofilos, S. Ves, M. P. Hehlen, N. L. Allan, C. E. Mohn and K. Papagelis, *J. Phys. Chem. Solids*, 2022, **162**, 110512.
46 W. Dewo, V. Gorbenko, A. Markovskyi, Y. Zorenko and T. Runka, *J. Lumin.*, 2023, **254**, 119481.
47 A. Lukowiak, R. J. Wiglusz, M. Maczka, P. Gluchowski and W. Strek, *Chem. Phys. Lett.*, 2010, **494**, 279–283.
48 K. Eremeev, P. Loiko, A. Braud, P. Camy, J. Zhang, X. Xu, Y. Zhao, P. Liu, S. Balabanov, E. Dunina, A. Kornienko, L. Fomicheva, X. Mateos, U. Griebner, V. Petrov, L. Wang and W. Chen, *Opt. Mater. Express*, 2022, **12**, 3749–3762.
49 J. Li, W. Hou, X. Xu, Y. Xue, Q. Song, J. Liu, F. Wu, P. Luo, F. Wang, H. Yu, Q. Wang and J. Xu, *Opt. Mater. Express*, 2022, **12**, 3071–3080.
50 E. Dobretsova, O. Alimov, D. Guryev, V. Voronov, S. Rusanov, V. Kashin, S. Kutovoy, V. Vlasov, L. Badyanova, I. Novikov and V. Tsvetkov, *Crystals*, 2022, **12**, 1745.
51 R. N. Maksimov, G. Toci, A. Pirri, V. A. Shitov, E. Sani, A. Santonocito, B. Patrizi, M. Becucci, M. Vannini and V. V. Osipov, *Opt. Mater.*, 2024, **151**, 115309.
52 O. Alimov, E. Dobretsova, D. Guryev, V. Kashin, G. Kiriukhina, S. Kutovoi, S. Rusanov, S. Simonov, V. Tsvetkov, V. Vlasov, V. Voronov and O. Yakubovich, *Cryst. Growth Des.*, 2020, **20**, 4593–4599.
53 V. M. Goldschmidt, *Die Naturwissenschaften*, 1926, **14**, 477–485.
54 A. Casu and P. C. Ricci, *J. Solid State Chem.*, 2011, **184**, 3028–3033.
55 W. Dewo, V. Gorbenko, Y. Syrotych, Y. Zorenko and T. Runka, *J. Phys. Chem. C*, 2021, **125**, 16279–16288.
56 A. Chopelas, *Phys. Chem. Miner.*, 2011, **38**, 709–726.
57 J. L. Wu, J. J. Wang, X. Y. Zhang, F. Liang, D. Z. Lu, S. H. Ma, Z. G. Hu, N. Ye and J. Y. Wang, *Infrared Phys. Technol.*, 2023, **135**, 104976.
58 A. B. Muñoz-García, Z. Barandiarán and L. Seijo, *J. Mater. Chem.*, 2012, **22**, 19888–19897.
59 J. Pejchal, M. Nikl, E. Mihóková, J. A. Mareš, A. Yoshikawa, H. Ogino, K. M. Schillemat, A. Krasnikov, A. Vedda, K. Nejezchleb, V. Múčka, J. Pejchal, M. Nikl, E. Mihóková, J. A. Mareš, A. Yoshikawa, H. Ogino, K. M. Schillemat, A. Krasnikov, A. Vedda, K. Nejezchleb and V. Múčka, *J. Phys. D: Appl. Phys.*, 2009, **42**, 055117.
60 A. M. Srivastava, *J. Lumin.*, 2016, **169**, 445–449.
61 W. Guo, B. Jiang, J. Zhu, L. Zhang, W. Guo, B. Jiang, J. Zhu and L. Zhang, *Crystals*, 2021, **11**, 1433.
62 R. H. Bartram, D. S. Hamilton, L. A. Kappers and A. Lempicki, *J. Lumin.*, 1997, **75**, 183–192.
63 V. M. Khanin, I. Venevtsev, K. Chernenko, T. Tukhvatulina, P. A. Rodnyi, S. Spoor, J. Boerekamp, A.-M. van Dongen, D. Buettner, H. Wieczorek, C. R. Ronda, T. Senden and A. Meijerink, *Cryst. Growth Des.*, 2020, **20**, 3007–3017.
64 M. Nikl, A. Vedda, M. Fasoli, I. Fontana, V. V. Laguta, E. Mihokova, J. Pejchal, J. Rosa and K. Nejezchleb, *Phys. Rev. B:Condens. Matter Mater. Phys.*, 2007, **76**, 195121.
65 E. McGlynn, *Contemp. Phys.*, 2013, **54**, 115–116.
66 A. B. Abragam, *Electron Paramagnetic Resonance of Transition Ions*, Oxford University Press, London, England, 2012.
67 S. K. Misra and L. E. Misiak, *Phys. Rev. B:Condens. Matter Mater. Phys.*, 1993, **48**, 13579–13587.
68 A. Nakatsuka, A. Yoshiasa and T. Yamanaka, *Acta Crystallogr., Sect. B:Struct. Sci.*, 1999, **55**, 266–272.
69 J. R. B. J. E. Wertz, *Electron Spin Resonance: Elementary Theory and Practical Applications*, Chapman and Hall, New York, 1986.

